THE PHOTOREFRACTIVE EFFECT IN $LiNbO_3$

By

MICHAEL LYNN KLIEWER

Bachelor of Science in Mechanical Engineering

Oklahoma State University

Stillwater, Oklahoma

1983

Submitted to the Faculty of the Graduate College
of the Oklahoma State University
in partial fulfillment of the requirements
for the Degree of
MASTER OF SCIENCE
May, 1986

THE PHOTOREFRACTIVE EFFECT IN $LiNbO_3$

Thesis Approved:

Richard C. Powell
Thesis Adviser

Larry E. Halliburton

W. A. Sibley

Norman N. Durham
Dean of the Graduate College

ACKNOWLEDGMENTS

I would like to express my gratitude to all the people responsible for helping me during my studies at Oklahoma State University and for assisting me in completing my thesis. Foremost among these is Dr. Richard C. Powell. Dr. Powell gave me the opportunity to work in his research laboratory. The experience and knowledge received has become invaluable. I also thank him for being an excellent adviser, committee Chairman, and mostly, for being a good friend. I would also like to thank the other members on my committee, Dr. William A. Sibley and Dr. Larry E. Halliburton, for their assistance. Thanks also goes to Jacek K. Tyminski and H. C. Chow for their assistance. Further, I would like to thank Mrs. Dee Behrens for her expert typing of this thesis.

My special thanks and love go to my parents, my brother, and all my family for their love, support, and understanding throughout my life, and especially while attending Oklahoma State University. Finally, I thank God for blessing me with a healthy body and mind and providing me with the strength needed.

Financial support for this work was provided by the U. S. Army Research Office and by the National Science Foundation under Grant No. DMR-82-16551.

TABLE OF CONTENTS

LIST OF FIGURES

CHAPTER I

INTRODUCTION

The Photorefractive Effect in $LiNbO_3$

Creating laser-induced refractive-index changes [Photorefractive Effect (PRE)] in $LiNbO_3$ crystals has been an important topic in research for many years [1-4]. The photorefractive effect is crucial for material used in applications requiring the transmission of laser beams because the refractive index changes act as optical damage centers [5,6]. In addition, holographic images can be formed through the PRE for optical storage and for establishing gratings used in phase conjugation and beam scattering. Therefore, it is important to have a detailed understanding of the physical processes underlying the PRE so materials can be produced with optimum characteristics.

Photorefractive patterns in the form of gratings can be produced in materials using crossed laser beams. This is called the holographic technique. Information concerning the holographic grating can then be extracted using various methods. One such method is to monitor the efficiency of scattering a laser probe beam off of the grating at the Bragg diffraction angle. Another method is to measure the decay time of the scattering efficiency while the grating is being erased by another source of light. It is assumed that the grating formed during the holographic technique is in the form of a purely sinusoidal pattern with a

well defined Bragg condition so that the theoretical analysis of the data gives the modulation or grating depth of the refractive index grating. The properties of the charge carrier generation, dynamics of relocation, and trapping underlying the PRE that produces the grating can be determined by measuring the changes in scattering efficiency. These changes in scattering efficiency occur when properties such as defect content or temperature of the sample are changed or when experimental conditions such as grating spacing or erasure beam are changed.

One problem with the experimental method described above is that absolute measurements of scattering efficiencies are not very precise. Inaccuracies occur because of additional surface and bulk scattering processes as well as limitation due to the angular distribution of the fields present in the probe and scattered beams. Nonlinearities in the photorefractive grating produce complex grating shapes instead of pure sinusoidal gratings. Although advances have been made in obtaining fundamental properties of the charge carrier-defect dynamics in some photorefractive materials, [7-9] there is still much to be understood about these processes which are nonlinear due to the coupling between the electrostatic field and the migrating charges. Nonlinearities of the charge relocation within the volume of the crossed Gaussian beams make the assumption of a purely sinusoidal grating with a well defined Bragg condition highly questionable for most conditions and the exact thickness of the grating is difficult to determine. A new technique is needed to account for a nonsinusoidal grating and that will give accurate values for the grating depth and grating thickness. The goal of this study is to develop an expression to describe the diffraction efficiency of light by a nonlinear optical material. From this

expression, values for the grating depth and grating thickness can be obtained for various doped and undoped crystals of $LiNbO_3$.

Summary of Thesis

In this study, the properties of the photorefractive effect were investigated using the holographic grating technique in doped and undoped nominally pure $LiNbO_3$ crystals. Gratings were created with different write beam crossing angles between 2.5° and 8.0° and the angular distributions of the scattered probe beam intensity were measured. Scattering maxima were observed at several different angles and each spot was found to have a different erasure decay rate. This is attributed to diffraction from a complex grating having multiple Fourier components. A theoretical method is presented for analyzing these types of data and obtaining information concerning the refractive index modulation of each component of the grating. In addition, computer fits of small angle scattering patterns for each diffraction maximum are shown to provide very accurate values of the grating depth and thickness. A comparison is made between results obtained from this technique and those obtained by measurements of the scattering efficiency at the Bragg angle with special attention focused on the importance of beam geometries in laser-induced grating experiments.

CHAPTER II

THEORETICAL DEVELOPMENT

In this section the expression describing the diffraction efficiency of light by a nonlinear optical material whose dielectric constant and conductivity are aperiodically spatially modulated is derived. In general, the aperiodic modulation of the material constants cannot be accurately described by a simple sinusoidal pattern with a single spacial frequency. A better description of complex gratings is to use the superposition of several sinusoidal patterns with different grating vectors. If two or more grating vectors are present simultaneously, it is impossible for a given incident beam to satisfy Bragg condition for all of the grating vectors at the same time. Kogelnik [10] analyzed light scattering off Bragg's condition for the case of a single grating vector. It is important to determine if his results are valid for the different diffraction maxima which appear for multicomponent gratings. The subject of this section is to go beyond the level of accuracy developed by Kogelnik by considering the diffraction of a nonsinusoidal grating. Roughly speaking, the basic qualitative conclusion of the present study is as follows: If the modulated index of refraction pattern is resolved into its Fourier components as characterized by different grating vectors, then under Bragg condition for a given grating vector the diffracted light is largely independent of the other grating vectors. Off Bragg condition, the diffraction pattern is influenced by the presence

of other grating vectors. Experimental observations substantiate this feature. Insofar as the present study represents an extension of Kogelnik's theory [10], his notations will be followed with as slight modifications as possible. In this study, i will be used whereas in Kogelnik's theory, j = -i is used. Equations are in MKS units.

The situation to be studied is shown schematically in Figure 1. An incident light beam R is brought into a medium containing a photorefractive grating. The average dielectric constant and conductivity of the medium are ε and σ, respectively. Choose the z-axis normal to the surface of the medium and the x-axis in the plane of incidence. Let the material be infinite in extent in the y-direction so that no physical quantities will have a y-dependence. The incident light enters a region ($0 \leq z \leq d$) where the material constants are modulated and emerges as S_1, S_2 after suffering changes in the propagation direction.

Actually the experiments to which the theory is intended to apply can be carried out during the erasure time of the grating. This means that the dielectric constant and conductivity of the medium are not only spatially modulated but can also be time-dependent. Under these circumstances Maxwell's equations together with Ohm's law dictate the behavior of the electric field $\vec{E}$ associated with the light.

$$\vec{\nabla} \times \vec{E} = - \frac{\partial B}{\partial t} \tag{1}$$

$$\vec{\nabla} \times (\vec{\nabla} \times \vec{E}) = \vec{\nabla} \times \left(- \frac{\partial B}{\partial t} \right) \tag{2}$$

$$\vec{\nabla} (\vec{\nabla} \cdot \vec{E}) - \nabla^2 \vec{E} = - \frac{\partial}{\partial t} (\vec{\nabla} \times \vec{B}) \tag{3}$$

$$-\nabla^2 E = - \frac{\partial}{\partial t} (\mu J + \mu \frac{\partial}{\partial t} (\varepsilon \vec{E})) \tag{4}$$

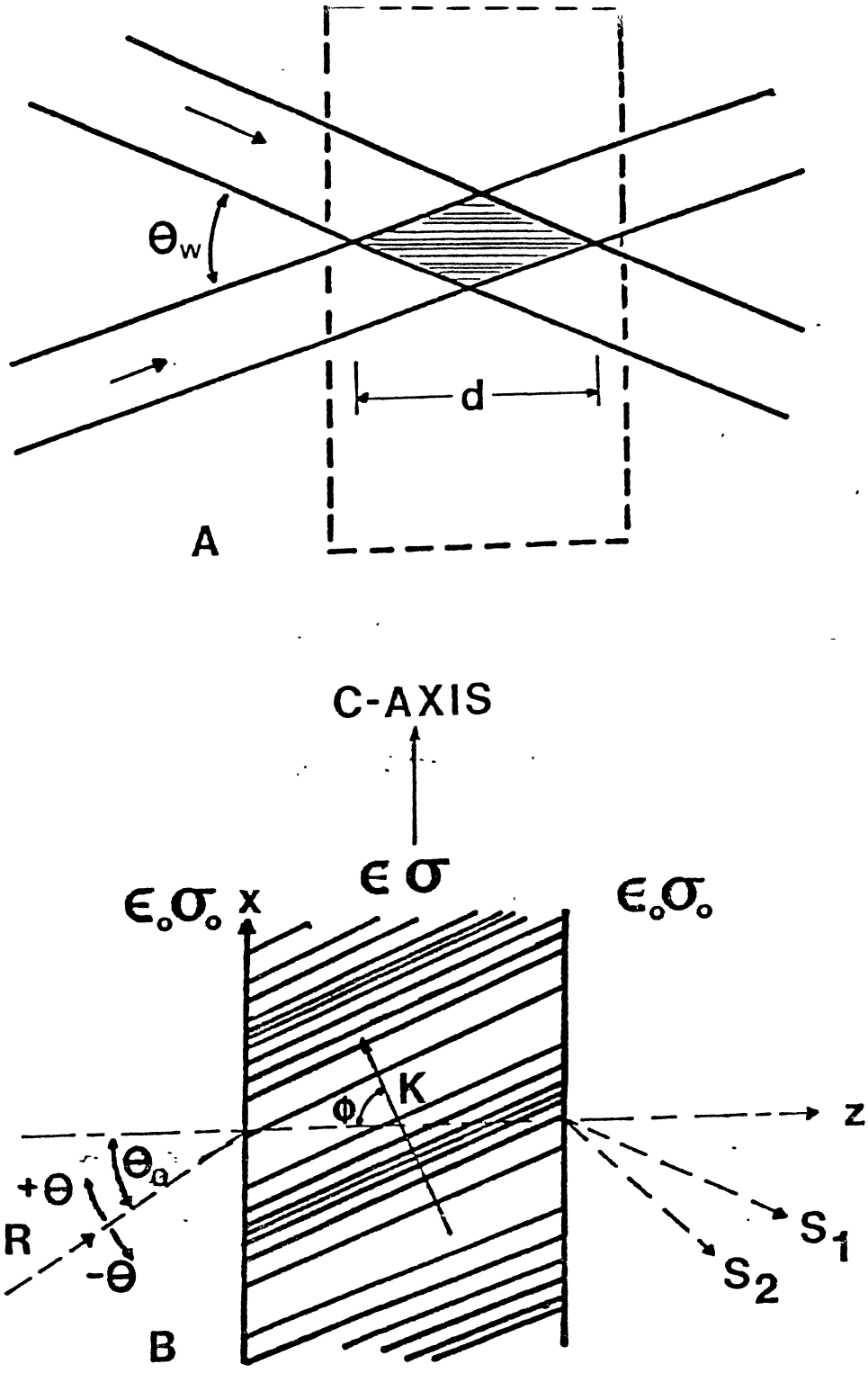

Figure 1. Beam Geometry for Writing and Reading Laser-Induced Gratings

$$\nabla^2 E - \frac{\partial}{\partial t}\left(\mu\sigma\vec{E} + \mu\frac{\partial}{\partial t}(\varepsilon\vec{E})\right) = 0 \tag{5}$$

$$\nabla^2 E - \frac{\partial}{\partial t}\left(\mu\sigma\vec{E} + \mu\left(\varepsilon\frac{\partial\vec{E}}{\partial t} + \vec{E}\frac{\partial\varepsilon}{\partial t}\right)\right) = 0 \tag{6}$$

$$\nabla^2 E - \mu\sigma\frac{\partial\vec{E}}{\partial t} - \mu\frac{\partial\sigma}{\partial t}\vec{E} - \mu\left(\frac{\partial\varepsilon}{\partial t}\right)\left(\frac{\partial\vec{E}}{\partial t}\right) - \mu\varepsilon\frac{\partial^2\vec{E}}{\partial t^2} - \mu\left(\frac{\partial\vec{E}}{\partial t}\right)\left(\frac{\partial\varepsilon}{\partial t}\right) - \mu\vec{E}\frac{\partial^2\varepsilon}{\partial t^2} = 0 \tag{7}$$

$$\nabla^2\vec{E} - \mu\sigma\frac{\partial\vec{E}}{\partial t} - \mu\frac{\partial\sigma}{\partial t}\vec{E} - \mu\varepsilon\frac{\partial^2\vec{E}}{\partial t^2} - 2\mu\left(\frac{\partial\varepsilon}{\partial t}\right)\left(\frac{\partial\vec{E}}{\partial t}\right) - \mu\frac{\partial^2\varepsilon}{\partial t^2}\vec{E} = 0 \tag{8}$$

where μ, σ, and ε are respectively the permeability, conductivity, and dielectric constant of the medium. If the $\vec{E}$ field is monochromatic with an angular frequency ω, and the time variations of the dielectric constant and the conductivity are slow in comparison with time variations of the field, then in Equation (8) the third and last two terms may be disregarded. Equation (8) becomes

$$\nabla^2 E - \mu\sigma\frac{\partial\vec{E}}{\partial t} - \mu\varepsilon\frac{\partial^2 E}{\partial t^2} = 0 \tag{9}$$

If, in addition, the incident light is polarized perpendicular to the plane of incidence, only the y-component of the $\vec{E}$-field, denoted by $E(x,z)$ will be of interest.

$$\nabla^2\vec{E} + i\mu\sigma\omega\vec{E} - \mu\varepsilon\omega^2\vec{E} = 0 \tag{10}$$

This obeys the Helmholtz equation

$$(\nabla^2 + k^2)E(x,z) = 0 \tag{11}$$

where the complex propagation constant k is given by

$$k^2 = \mu\varepsilon\omega^2 + i\mu\sigma\omega. \tag{12}$$

The dielectric constant and conductivity in the modulated region are written respectively as

$$\varepsilon = \varepsilon_o + \sum_{i=1}^{N} \varepsilon_i \cos\vec{K}_i \cdot \vec{x} \tag{13}$$

$$\sigma = \sigma_o + \sum_{i=1}^{N} \sigma_i \cos\vec{K}_i \cdot \vec{x} \tag{14}$$

where the summation over i contains the N terms needed to describe the grating modulation, $\vec{x} = (x,y,z)$ is a position vector, $\vec{K}_i = K_i(\sin\phi_i, 0, \cos\phi_i)$ is the grating vector of the i^{th} modulation component, and ε_i and σ_i are the cosine transforms associated with the $\vec{K}_i$ contribution to the spatial modulation of the dielectric constant and conductivity, respectively, and may themselves be time-dependent (albeit slowly compared with the field time-variation).

Modifications of the index of refraction and the absorption constant of the medium are related to these modulations. The index of refraction can be written as

$$n = n_o + \sum_{i=1}^{N} \Delta n_i \cos\left(\vec{K}_i \cdot \vec{x}\right) \tag{15}$$

where n_o is the average value and Δn_i is the change in the index of refraction due to the i^{th} modulation. In a similar manner, the absorption constant can be written as

$$\alpha = \alpha_o + \sum_{i=1}^{N} \Delta\alpha_i \cos\left(\vec{K}_i \cdot \vec{x}\right). \tag{16}$$

Under conditions of weak modulation,

$$n_o \approx \varepsilon_o^{1/2}; \qquad \Delta n_i \approx \frac{\varepsilon_i}{2\varepsilon_o^{1/2}} \tag{17}$$

and

$$\alpha_o = \frac{c\mu\sigma_o}{2\varepsilon_o^{1/2}}; \qquad \Delta\alpha = \frac{c\mu\sigma_i}{2\varepsilon_o^{1/2}} . \tag{18}$$

Upon introducing the average propagation constant β via

$$\beta = \frac{2\pi\varepsilon_o^{1/2}}{\lambda} \quad , \quad \approx \frac{2\pi n_o}{\lambda} \tag{19}$$

where λ is the wavelength in a vacuum, and the coupling constants κ_i via

$$\kappa_i = (1/4)\left[\frac{2\pi\varepsilon_i}{(\lambda\varepsilon_o^{1/2})} + i\,\frac{c\mu\sigma_i}{\varepsilon_o^{1/2}}\right] \approx \frac{\pi\Delta n_i}{\lambda} + i\,\frac{\Delta\alpha_i}{2} \tag{20}$$

The coupling constants describe the coupling between the reference wave R and the signal wave S. For $\kappa = 0$ there is no coupling between R and S, thus no diffraction. Equation (12) may be rewritten

$$k^2 = \mu\varepsilon\omega^2 + i\mu\sigma\omega \tag{21}$$

$$k^2 = \frac{\mu\varepsilon 4\pi^2 c^2}{n^2\lambda^2} + \frac{ic\mu\sigma\omega}{c} \tag{22}$$

$$k^2 = \frac{4\pi^2\varepsilon}{\lambda^2} + \frac{ic\mu\omega\sigma}{\nu\lambda} \tag{23}$$

$$k^2 = \frac{4\pi^2\varepsilon}{\lambda^2} + \frac{2\pi ic\mu\sigma}{\lambda} \tag{24}$$

$$k^2 = \frac{2\pi}{\lambda}\left[\frac{2\pi\hat{\varepsilon}}{\lambda} + ic\mu\sigma - ic\mu\sigma_o + ic\mu\sigma_o\right] \tag{25}$$

$$k^2 = \frac{2\pi}{\lambda}\left[\frac{2\pi\varepsilon}{\lambda} + ic\mu\sigma - ic\mu\sigma_o + ic\mu\,\frac{2\alpha_o\varepsilon_o^{1/2}}{c\mu}\right] \tag{26}$$

$$k^2 = \frac{2\pi}{\lambda}\left[\frac{2\pi\varepsilon}{\lambda} - \frac{2\pi\varepsilon_o}{\lambda} + \frac{2\pi\varepsilon_o}{\lambda} - ic\mu\sigma_o + ic\mu\sigma + 2i\alpha_o\varepsilon_o^{1/2}\right] \tag{27}$$

$$k^2 = \frac{2\pi}{\lambda}\left[\frac{2\pi}{\lambda}(\varepsilon-\varepsilon_o) + \frac{2\pi\varepsilon_o}{\lambda} + ic\mu(\sigma-\sigma_o) + 2i\alpha_o\varepsilon_o^{1/2}\right] \tag{28}$$

$$k^2 = \frac{2\pi}{\lambda}\left[\frac{2\pi}{\lambda}\varepsilon_i\cos(\vec{K}_i\cdot\vec{x}) + \frac{2\pi\varepsilon_o}{\lambda} + ic\mu\sigma_i\cos(\vec{K}_i\cdot\vec{x}) + 2i\alpha_o\varepsilon_o^{1/2}\right] \tag{29}$$

$$k^2 = \frac{4\pi^2\varepsilon_o}{\lambda^2} + \frac{4\pi i\alpha_o\varepsilon_o^{1/2}}{\lambda} + \frac{4\pi^2}{\lambda^2}\varepsilon_i\cos(\vec{K}_i\cdot\vec{x}) + \frac{2\pi ic\mu}{\lambda}\sigma_i\cos(\vec{K}_i\cdot\vec{x}) \tag{30}$$

$$k^2 = \frac{4\pi^2\varepsilon_o}{\lambda^2} + \frac{4\pi i\alpha_o\varepsilon_o^{1/2}}{\lambda} + \left[\frac{4\pi^2}{\lambda^2}\varepsilon_i + \frac{2\pi ic\mu\sigma_i}{\lambda}\right]\cos(\vec{K}_i\cdot\vec{x}) \tag{31}$$

$$k^2 = \frac{4\pi^2\varepsilon_o}{\lambda^2} + \frac{4\pi i\alpha_o\varepsilon_o^{1/2}}{\lambda} + \left[\frac{2\pi\varepsilon_o^{1/2}}{\lambda}\left(\frac{2\pi\varepsilon_i}{\varepsilon_o^{1/2}\lambda}\right) + \frac{2\pi\varepsilon_o^{1/2}}{\lambda}\left(\frac{ic\mu\sigma_i}{\varepsilon_o^{1/2}\lambda}\right)\right]\cos(\vec{K}_i\cdot\vec{x}) \tag{32}$$

$$k^2 = \frac{4\pi^2\varepsilon_o}{\lambda^2} + \frac{4\pi i\alpha_o\varepsilon_o^{1/2}}{\lambda} + \frac{2\pi\varepsilon_o^{1/2}}{\lambda}\left[\frac{2\pi\varepsilon_i}{\lambda\varepsilon_o^{1/2}} + \frac{ic\mu\sigma_i}{\lambda\varepsilon_o^{1/2}}\right]\cos(\vec{K}_i\cdot\vec{x}) \tag{33}$$

$$k^2 = \frac{4\pi^2\varepsilon_o}{\lambda^2} + \frac{4\pi i\alpha_o\varepsilon_o^{1/2}}{\lambda} + \frac{8\pi\varepsilon_o^{1/2}}{\lambda}\left(\frac{1}{4}\right)\left[\frac{2\pi\varepsilon_i}{\lambda\varepsilon_o^{1/2}} + \frac{ic\mu\sigma_i}{\varepsilon_o^{1/2}}\right]\cos(\vec{K}_i\cdot\vec{x}) \tag{34}$$

$$k^2 = \frac{4\pi^2\varepsilon_o}{\lambda^2} + \frac{4\pi i\alpha_o\varepsilon_o^{1/2}}{\lambda} + \frac{8\pi\varepsilon_o^{1/2}}{\lambda}\sum_{i=1}^{N}\kappa_i\cos(\vec{K}_i\cdot\vec{x}) \tag{35}$$

$$k^2 = \beta^2 + \frac{4\pi i\alpha_o\varepsilon_o^{1/2}}{\lambda} + \frac{4\pi\varepsilon_o^{1/2}}{\lambda}\sum_{i=1}^{N}\kappa_i 2\cos(\vec{K}_i\cdot\vec{x}) \tag{36}$$

$$k^2 = \beta^2 + \frac{4\pi i\alpha_o\varepsilon_o^{1/2}}{\lambda} + \frac{4\pi\varepsilon_o^{1/2}}{\lambda}\sum_{i=1}^{N}\kappa_i\left[e^{i\vec{K}_i\cdot\vec{x}} + e^{-i\vec{K}_i\cdot\vec{x}}\right] \tag{37}$$

$$k^2 = \beta^2 + 2i\alpha_o\left(\frac{2\pi\varepsilon_o^{1/2}}{\lambda}\right) + \left(\frac{2\pi\varepsilon_o^{1/2}}{\lambda}\right)\sum_{i=1}^{N}2\kappa_i\left[e^{i\vec{K}_i\cdot\vec{x}} + e^{-i\vec{K}_i\cdot\vec{x}}\right] \tag{38}$$

$$k^2 = \beta^2 + 2i\alpha_o\beta + \beta\sum_{i=1}^{N}2\kappa_i\left[e^{i\vec{K}_i\cdot\vec{x}} + e^{-i\vec{K}_i\cdot\vec{x}}\right] \tag{39}$$

$$k^2 = \beta^2 + 2i\alpha_o\beta + \sum_{i=1}^{N}2\beta\kappa_i\left[e^{i\vec{K}_i\cdot\vec{x}} + e^{-i\vec{K}_i\cdot\vec{x}}\right] \tag{40}$$

The electric field inside the modulated region of the photorefractive material is the superposition of the incident and diffracted waves:

$$E = R(z)e^{i\vec{r}\cdot\vec{x}} + \sum_{i=1}^{N} S_i(z)e^{i\vec{s}_i\cdot\vec{x}} . \tag{41}$$

Here $\vec{r} = \beta\ (\sin\theta,\ 0,\ \cos\theta)$ is the propagation vector of the incident wave, $\vec{s}_i$ are the propagation vectors associated with the diffracted waves and are related to the incident wave vector through the grating vector $\vec{K}_i$,

$$\vec{s}_i = \vec{r}_i - \vec{K}_i \tag{42}$$

with Cartesian components $(\beta\sin\phi - K_i\sin\phi_i,\ 0,\ \beta\cos\theta - K_i\cos\phi_i)$. The condition for exact Bragg scattering for grating vector $\vec{K}_i$ is specified by

$$2\beta\cos(\phi_i - \theta_B) = K_i \tag{43}$$

for angle $\theta = \theta_B$. A convenient measure of the departure from this exact condition is given by the dephasing parameters ζ_i defined by

$$\zeta_i = \frac{(\beta^2 - s_i^2)}{2\beta} . \tag{44}$$

These are zero at exact Bragg condition for $\vec{K}_i$.

Now substitute Equations (40) and (41) into Equation (11).

$$\nabla^2 E + k^2 E = 0$$

$$\nabla^2 E + \left(\beta^2 + 2i\alpha_o\beta + 2\beta\sum_{i=1}^{N}\kappa_i e^{i\vec{K}\cdot\vec{x}} + 2\beta\sum_{i=1}^{N}\kappa_i e^{-i\vec{K}\cdot\vec{x}}\right)\left[R(z)e^{i\vec{r}\cdot\vec{x}} + S_i(z)e^{i\vec{s}\cdot\vec{x}}\right] = 0 \tag{45}$$

$$\nabla^2 E + \beta^2 R(z) e^{i\vec{r}\cdot\vec{x}} + \beta^2 \sum_{i=1}^{N} S_i(z) e^{i\vec{s}\cdot\vec{x}} + 2i\alpha_o \beta R(z) e^{i\vec{r}\cdot\vec{x}} +$$

$$2i\alpha_o \beta \sum_{i=1}^{N} S_i(z) e^{i\vec{s}\cdot\vec{x}} + 2\beta \sum_{i=1}^{N} \kappa_i R(z) e^{i(\vec{K}+\vec{r})\cdot\vec{s}} + 2\beta \sum_{i=1}^{N} \kappa_i S_i(z) e^{i(\vec{s}+\vec{K}_i)\cdot x}$$

$$2\beta \sum_{i=1}^{N} \kappa_i R(z) e^{i(-\vec{K}+\vec{r})\cdot\vec{x}} + 2\beta \sum_{i=1}^{N} \kappa_i S_i(z) e^{-i(-\vec{K}+\vec{s})\cdot\vec{x}} = 0 \qquad (46)$$

$$\nabla^2 E + \beta^2 R(z) e^{i\vec{r}\cdot\vec{x}} + \beta^2 S_i(z) e^{i\vec{s}\cdot\vec{x}} + 2i\alpha_o \beta R(z) e^{i\vec{r}\cdot\vec{x}} + 2i\alpha_o \beta S_i(z) e^{i\vec{s}\cdot\vec{x}} +$$

$$2\beta \sum_{i=1}^{N} \kappa_i R(z) e^{i(\vec{r}-\vec{s}+\vec{r})\cdot\vec{x}} + 2\beta \sum_{i=1}^{N} \kappa_i S_i(z) e^{i(\vec{r}-\vec{s}+\vec{s})\cdot\vec{x}} +$$

$$2\beta \sum_{i=1}^{N} \kappa_i R(z) e^{-i(\vec{s}-\vec{r}+\vec{r})\cdot\vec{x}} + 2\beta \sum_{i=1}^{N} \kappa_i S_i(z) e^{-i(\vec{s}-\vec{r}+\vec{s})\cdot\vec{x}} = 0 \qquad (47)$$

$$\left[R'' + 2ir_z R' - R r_z^2\right] e^{i\vec{r}\cdot\vec{x}} + \left[S_i'' + 2is_z S_i' - S_i s_z^2\right] e^{i\vec{s}\cdot\vec{x}} +$$

$$\beta^2 R(z) e^{i\vec{r}\cdot\vec{x}} + \beta^2 S_i(z) e^{i\vec{s}\cdot\vec{x}} + 2i\alpha_o \beta R(z) e^{i\vec{r}\cdot\vec{x}} +$$

$$2i\alpha_o \beta S_i(z) e^{i\vec{s}\cdot\vec{x}} + 2\beta \sum_{i=1}^{N} \kappa_i R(z) e^{i2\vec{r}\cdot\vec{x}} e^{-i\vec{s}\cdot\vec{x}} + 2\beta \sum_{i=1}^{N} \kappa_i S_i(z) e^{i\vec{r}\cdot\vec{x}} +$$

$$2\beta \sum_{i=1}^{N} \kappa_i R(z) e^{-i\vec{s}\cdot\vec{x}} + 2\beta \sum_{i=1}^{N} \kappa_i S_i(z) e^{i\vec{r}\cdot\vec{x}} e^{-2i\vec{s}\cdot\vec{x}} = 0 \qquad (48)$$

The seventh and tenth terms are neglected because they oscillate too fast and average out to zero. After comparing the terms proportional to $\exp(i\vec{r}\cdot\vec{x})$ and $\exp(i\vec{s}\cdot\vec{x})$, the equations for the complex wave amplitudes become

$$R'' + 2ir_z R' + 2i\alpha_o \beta R + (\beta^2 - r_z^2) R + 2\beta \sum_{i=1}^{N} \kappa_i S_i = 0 \qquad (49)$$

$$S_i'' + 2is_{iz} S_i' + 2i\alpha_o \beta S_i + (\beta^2 - s_i^2) S_i + 2\kappa_i \beta R = 0 \qquad (50)$$

where i runs from 1 to N and the primes indicate derivatives with respect to z. In Equation (49) the fourth term goes to zero because the incident beam is normal to the sample. Equations (49) and (50) indicate that the energies associated with the incident and diffracted waves can be depleted through absorption. Also indicated is that there is a direct energy interchange between the incident and diffracted waves through the coupling constants while there is only an indirect energy interchange between the diffracted waves through sharing the same incident wave (R). As in Kogelinik's analysis [10], the second space derivatives of the R and S_i fields are neglected. This is justified insofar as the field envelopes change slowly. Neglecting the second derivatives leaves a set of differential equations of the form

$$2ir_z R' + 2i\alpha_o \beta R + 2\beta_i \sum_{i=1}^{N} \kappa_i S_i = 0 \qquad (51)$$

$$2is_{iz} S_i' + 2i\alpha_o \beta S_i + (\beta^2 - s_i^2) S_i + 2\kappa_i \beta R = 0 \; . \qquad (52)$$

In Equation (51), the second term originates from the absorption of the fields propogating in the lossy medium and the third term describes the coupling between the incident (R) and scattering (S_i) fields. Similarly, in Equation (52) the second term is due to absorption, the third term is due to phase changes due to the wave diffracted from the grating, and the fourth term is due to the coupling between the R and S_i fields. The term describing the phase change due to diffraction reflects only directional relationships between probe, diffracted, and grating wave vectors. The terms describing the coupling between the R and S_i fields are dependent on the coupling constant κ_i. This coupling constant depends on the depth of both the real and imaginary parts of the index of refraction.

The validity of simplifying Equations (51) and (52) requires that the second derivative R" must be smaller than $2\beta_i \sum_{i=1}^{N} \kappa_i S_i$ and that the second derivative S_i'' must be smaller than $2\kappa_i \beta R$. These conditions set up a lower limit on the refraction index depth (or coupling parameter κ_i) for which Equations (51) and (52) can be used to give a physically meaningful description of observed diffraction patterns.

Letting $c_R = \frac{r_z}{\beta} = \cos\theta$ be the directional cosine with respect to the normal of the incident light, Equation (51) may be rewritten as

$$2ir_z R' + 2i\alpha_o \beta R + 2\beta_i \sum_{i=1}^{N} \kappa_i S_i = 0 \tag{53}$$

$$-ir_z R' - i\alpha_o \beta R + i^2 \beta_i \sum_{i=1}^{N} \kappa_i S_i = 0 \tag{54}$$

$$-r_z R' - \alpha_o \beta R = -i\beta_i \sum_{i=1}^{N} \kappa_i S_i \tag{55}$$

$$\frac{r_z}{\beta} R' + \alpha_o R = i_i \sum_{i=1}^{N} \kappa_i S_i \tag{56}$$

$$c_R R' + \alpha_o R = i \sum_{i=1}^{N} \kappa_i S_i \tag{57}$$

in a similar manner, defining $c_{S_i} = \frac{s_{iz}}{\beta} = \cos\theta - K_i \frac{\cos\phi}{\beta}$, Equation (52) may be rewritten as

$$2is_{iz} S_i' + 2i\alpha_o \beta S_i + (\beta^2 - s_i^2) S_i + 2\kappa_i \beta R = 0 \tag{58}$$

$$is_{iz} S_i' + i\alpha_o \beta S_i + \frac{\beta^2 - s_i^2}{2} S_i = -\kappa_i \beta R \tag{59}$$

$$\frac{s_{iz} S_i'}{\beta} + \alpha_o S_i - \frac{\beta^2 - s_i^2}{2\beta} iS_i = i\kappa_i R \tag{60}$$

$$c_{Si}S_i' + \left[\alpha_o - \frac{i}{2\beta}(\beta^2 - s_i^2)\right] S_i = i\kappa_i R \tag{61}$$

$$c_{Si}S_i' + (\alpha_o - i\zeta_i)S_i = i\kappa_i R, \qquad i = 1,2,\ldots,N \tag{62}$$

Equations (57) and (62) are supplemented with the boundary conditions

$$R(0) = 1, \qquad S_i(0) = 0, \qquad i = 1,2,\ldots,N \tag{63}$$

Equations (57), (62), and (63) constitute the basic equations for determining the diffraction efficiencies η_l in the directions of s_i. With the incident wave amplitude normalized to unity and the power flow being normal to the surface, the requisite diffraction efficiences are given by

$$\eta_i = \frac{c_{Si}}{c_R} S_i(d)S_i^*(d). \tag{64}$$

The requisite diffraction efficiencies are the fractional energy flows associated with the diffracted waves after emerging from the modulated region.

Since the shape of the grating is not known beforehand, the number of coupled differential equations in Equations (57) and (62) is unknown. Even if that were known and the required number of equations were solved exactly, the final results would be too complicated to be physically transparent and useful. It is therefore more advantageous to solve them approximately. The procedure for approximate solutions may be illustrated by considering the situation in which two grating vectors $\vec{K}_1$ and $\vec{K}_2$ are pertinent. The extension to other situations is obvious.

Two case may be distinguished. The first case occurs when one diffracted wave (say S_1) takes precedence over the other (S_2). This

happens if $\kappa_1 >> \kappa_2$, or when the coupling constants are comparable if the Bragg condition for $\vec{K}_1$ is nearly fulfilled. For this case it is permissible to ignore all the S_i terms in Equation (57) except for S_1. The resulting equation together with the two Equations (62) (for i = 1 and 2) can then be solved. The equations to solve are

$$c_R R' + \alpha_o R = i\kappa_1 S_1 \tag{65}$$

$$c_{S1} S_1' + (\alpha_o - i\zeta_1) S_1 = i\kappa_1 R \tag{66}$$

$$c_{S2} S_2' + (\alpha_o - i\zeta_2) S_2 = i\kappa_2 R \ . \tag{67}$$

Rewriting Equation (66) gives

$$R = \frac{-ic_{S1}}{\kappa} S_1' - i \frac{\alpha_o - i\zeta_1}{\kappa_1} S_1 \ . \tag{68}$$

Now substitute Equation (68) into Equation (65).

$$c_R \frac{-ic_{S1}}{\kappa_1} S_1'' - \frac{\alpha_o - i\zeta_1}{\kappa_1} iS_1' + \alpha_o \frac{-c_{S1}}{\kappa_1} iS_1' -$$

$$\frac{\alpha_o - i\zeta_1}{\kappa_1} iS_1 = i\kappa_1 S_1 \tag{69}$$

$$- \frac{ic_R c_{S1}}{\kappa_1} S_1'' - \frac{i\alpha_o c_R}{\kappa_1} S_1' - \frac{c_R \zeta_1}{\kappa} S_1' - \frac{ic_{S1}\alpha_o}{\kappa_1} S_1'$$

$$\frac{i\alpha_o^2}{\kappa_1} S_1 - \frac{\zeta\alpha_o}{\kappa_1} S_1 - i\kappa_1 S_1 = 0 \tag{70}$$

$$- \frac{c_R c_{S1}}{\kappa_1} S_1'' - \frac{\alpha_o c_R}{\kappa_1} S_1' + \frac{c_R i\zeta_1}{\kappa_1} S_1' - \frac{c_{S1}\alpha_o}{\kappa_1} S_1' -$$

$$\frac{\alpha_o^2}{\kappa_1} S_1 + \frac{i\zeta_1\alpha_o}{\kappa_1} S_1 - \kappa_1 S_1 = 0 \tag{71}$$

$$-(c_R c_{S1})S_1'' - (c_R\alpha_o + c_{S1}\alpha_o - c_R i\zeta_1)S_1' - (\alpha_o^2 - i\zeta_1\alpha_o + \kappa_1^2)S_1 = 0 \tag{72}$$

Assume a solution of the form $S_1(z) = Ae^{\lambda z}$ and substitute into Equation (72).

$$-\lambda^2(c_R c_{S1})Ae^{\lambda z} - \lambda(c_R\alpha_o + \alpha_o C_{S1} - i\zeta_1 c_R)Ae^{\lambda z} -$$

$$(\alpha_o^2 - i\zeta_1\alpha_o + \kappa_1^2)Ae^{\lambda z} = 0 \tag{73}$$

$$\lambda^2(c_R c_{S1}) + \lambda(c_R\alpha_o + \alpha_o c_{S1} - i\zeta_1 c_R) + (\alpha_o^2 - i\zeta_1\alpha_o - \kappa_1^2) = 0. \tag{74}$$

The quadratic equation will give solutions for λ.

$$\lambda = \frac{1}{2c_R c_{S1}} \left\{(-c_R\alpha_o - \alpha_o c_{S1} + i\zeta_1 c_R) \pm \left[(c_R\alpha_o + \alpha_o c_{S1} - i\zeta_1 c_R)^2 \right.\right.$$

$$\left.\left. -4(c_R C_{S1})(\alpha_o^2 - i\zeta_1\alpha_o + \kappa_1^2)^2\right]^{1/2}\right\} \tag{75}$$

$$\lambda = \frac{1}{2c_R c_{S1}} \left\{- c_R\alpha_o - c_{S1}\alpha_o + i\zeta_1 c_R \pm \left[c_R^2\alpha_o^2 + c_{S1}^2\alpha_o^2 - \right.\right.$$

$$\zeta_1^2 c_R^2 + 2\alpha_o^2 c_R c_{S1} - 2i\zeta\alpha_o c_R^2 - 2i\zeta_1\alpha_o c_R c_{S1} - 4c_R c_{S1}\alpha_o^2 +$$

$$\left.\left. 4c_R c_{S1} i\zeta\alpha_o - 4c_R c_{S1}\kappa_1^2\right]^{1/2}\right\} \tag{76}$$

$$\lambda = \frac{1}{2c_R c_{S1}} \left\{-c_R\alpha_o - C_{S1}\alpha_o + i\zeta_1 c_R \pm \left[(c_R^2\alpha_o^2 + c_{S1}^2\alpha_o^2 - \right.\right.$$

$$\left.\left. \zeta_1^2 c_R^2 - 2i\zeta\alpha_o c_R^2 - 2c_R c_{S1}\alpha_o^2 + 2c_R c_{S1} i\zeta\alpha_o) - 4c_R c_{S1}\kappa_1^2\right]^{1/2}\right\} \tag{77}$$

$$\lambda = \frac{1}{2c_R c_{S1}} \left\{-c_R\alpha_o - c_{S1}\alpha_o + i\zeta_1 c_R \pm \left[(c_R\alpha_o - c_{S1}\alpha_o - i\zeta_1 c_R)^2 - \right.\right.$$

$$\left.\left. 4c_R c_{S1}\kappa_1^2\right]^{1/2}\right\} \tag{78}$$

$$\lambda_{a,b} = \left(\frac{1}{2}\right)\left\{-\frac{\alpha_o}{c_{S1}} - \frac{\alpha_o}{c_R} + \frac{i\zeta_1}{c_{S1}} \pm \left[\left(\frac{\alpha_o}{c_{S1}} - \frac{\alpha_o}{c_R} - \frac{i\zeta_1}{c_{S1}}\right)^2 - \frac{4\kappa_1^2}{c_R c_{S1}}\right]^{1/2}\right\} \tag{79}$$

Using a more general solution, $S_1(z)$ may now be written as

$$S_1(z) = A_1 e^{\lambda_a z} + B_1 e^{\lambda_b z} . \tag{80}$$

Utilizing the boundary condition that $S_1(0) = 0$ enables the relationship between A_1 and B_1 to be determined ($A_1 = -B_1$). Therefore,

$$S_1(z) = B_1\left[e^{\lambda_b z} - e^{\lambda_a z}\right]. \tag{81}$$

Since in Equations (57) and (62) R is coupled to S, R must have the same general solution as S. This can be verified by following the same procedure to find R as was followed for S. Assuming a solution for R yields

$$R = A_2 e^{\lambda_a z} + B_2 e^{\lambda_b z} . \tag{82}$$

Utilizing the boundary condition that R(0) = 1 gives

$$1 = A_2 + B_2 \tag{83}$$

$$\lambda(z) = e^{\lambda_a z} + B_2\left[e^{\lambda_b z} - e^{\lambda_a z}\right] . \tag{84}$$

Evaluating Equations (65) and (66) at the boundary conditions gives the expression for $R'(0)$ and $S_1'(0)$.

$$R'(0) = \frac{-\alpha_o}{c_R} \tag{85}$$

$$S_1'(0) = \frac{i\kappa_1}{c_{S1}} . \tag{86}$$

Using the solution for $S_1(z)$ and the expression for $S_1'(0)$ allows for the coefficient B_1 to be found.

$$S_1'(0) = \frac{i\kappa_1}{c_{S1}} = B_1(\lambda_b - \lambda_a) \tag{87}$$

$$B_1 = \frac{-i\kappa_1}{c_{S1}(\lambda_a - \lambda_b)} \tag{88}$$

The solution for $S_1(z)$ is therefore,

$$S_1(z) = \frac{-i\kappa_1}{c_{S1}(\lambda_a - \lambda_b)} \left[e^{\lambda_b z} - e^{\lambda_a z} \right] \tag{89}$$

Similarly, for R(z) look at Equation (84) for the general solution for R(z) and evaluate the first derivative at z = 0.

$$R'(0) = \lambda_a + B_2(\lambda_b - \lambda_a) = \frac{-\alpha_o}{c_R} \tag{90}$$

$$B_2(\lambda_b - \lambda_a) = \frac{-1}{c_R}(\alpha_o + \lambda_a c_R) \tag{91}$$

$$B_2 = \frac{\alpha_o + \lambda_a c_R}{c_R(\lambda_a - \lambda_b)} \tag{92}$$

The solution for the incident wave R is

$$R(z) = e^{\lambda_a z} + \frac{\alpha_o + \lambda_a c_R}{c_R(\lambda_a - \lambda_b)} \left[e^{\lambda_b z} - e^{\lambda_a z} \right] \tag{93}$$

The solution for $S_2(z)$ is made up of both a particular ($S_{2P}(z)$) and homogeneous ($S_{2H}(z)$) solution. First find the homogeneous solution

$$C_{S2}S_2'(z) + (\alpha_o - i\zeta_2)S_2(z) = 0 \tag{94}$$

Assume a solution of the form $S_2(z) = A_3 e^{\Gamma z}$

$$\Gamma c_{S2} A_3 e^{\Gamma z} + (\alpha_o - i\zeta_2)A_3 e^{\Gamma z} = 0 \tag{95}$$

$$\Gamma = -\frac{(\alpha_o - i\zeta_2)}{c_{S2}} \tag{96}$$

so the homogeneous solution for $S_2(z)$ is

$$S_{2H}(z) = A_3 e^{\frac{(\alpha_o - i\zeta_2)z}{c_S}} . \tag{97}$$

Now find the particular solution. Assume a solution of the form

$$S_2(z) = De^{\lambda_a z} + Ge^{\lambda_b z} \tag{98}$$

and plug into Equation (67). Also substitute Equation (93) into Equation (67). Notice that Equation (98) is of the same form as the solution of R.

$$C_{S2}\left[\lambda_a De^{\lambda_a z} + \lambda_b Ge^{\lambda_b z}\right] + (\alpha_o - i\xi_2)\left[De^{\lambda_a z} + Ge^{\lambda_b z}\right] =$$

$$i\kappa_2\left\{e^{\lambda_a z} + \frac{(\alpha_o + \lambda_a c_R)}{c_R(\lambda_a - \lambda_b)}\left[e^{\lambda_b z} - e^{\lambda_a z}\right]\right\} \tag{99}$$

$$\lambda_a c_{S2} De^{\lambda_a z} + \lambda_b C_{S2} Ge^{\lambda_b z} + (\alpha_o - i\xi_2)De^{\lambda_a z} + (\alpha_o - i\zeta_2)Ge^{\lambda_b z} =$$

$$i\kappa_2 e^{\lambda_a z} + i\kappa_2 \frac{\alpha_o + \lambda_a c_R}{c_R(\lambda_a - \lambda_b)} e^{\lambda_b z} - i\kappa_2 \frac{\alpha_o + \lambda_a c_R}{c_R(\lambda_a - \lambda_b)} e^{\lambda_a z} \tag{100}$$

$$D(\lambda_a c_{S2} + \alpha_o - i\zeta_2)e^{\lambda_a z} + G(\lambda_b c_{S2} + \alpha_o - i\zeta_2)e^{\lambda_b z} =$$

$$\left[i\kappa_2 - i\kappa_2 \frac{\alpha_o + c_R\lambda_a}{c_R(\lambda_a - \lambda_b)}\right]e^{\lambda_a z} + i\kappa_2\left[\frac{\alpha_o + \lambda_a c_R}{c_R(\lambda_a - \lambda_b)}\right]e^{\lambda_b z} \tag{101}$$

the coefficients D and G can be found by equating the coefficients of the exponential power $\lambda_a z$ and $\lambda_b z$. First look at D.

$$D(\lambda_a c_{S2} + \alpha_o - i\zeta_2) = \frac{i\kappa_2 c_R(\lambda_a - \lambda_b) - i\kappa_2(\alpha_o + \lambda_a c_R)}{c_R(\lambda_a - \lambda_b)} \tag{102}$$

$$D = \frac{i\kappa_2 c_R\lambda_a - i\kappa_2 c_R\lambda_b - i\kappa_2\alpha_o - i\kappa_2\lambda_a c_R}{(\lambda_a c_{S2} + \alpha_o - i\zeta_2)c_R(\lambda_a - \lambda_b)} \tag{103}$$

$$D = \frac{-i\kappa_2}{c_R(\lambda_a - \lambda_b)} \quad \frac{\alpha_o + c_R\lambda_b}{c_{S2}\lambda_a + \alpha_o - i\zeta_2} \tag{104}$$

Now solve for G in the same manner.

$$G(\lambda_b c_{S2} + \alpha_o - i\zeta_2) = \frac{i\kappa_2(\alpha_o + \lambda_a c_R)}{c_R(\lambda_a - \lambda_b)} \tag{105}$$

$$G = \frac{i\kappa_2(\alpha_o + \lambda_a c_R)}{c_R(\lambda_a - \lambda_b)(\lambda_b c_{S2} + \alpha_o - i\zeta_2)} \tag{106}$$

$$G = \frac{i\kappa_2}{c_R(\lambda_a - \lambda_b)} \quad \frac{\alpha_o + \lambda_a c_R}{c_{S2}\lambda_b + \alpha_o - i\zeta_2} \tag{107}$$

The particular soltuion for $S_2(z)$ is therefore

$$S_{2P}(z) = \frac{-i\kappa_2}{c_R(\lambda_a - \lambda_b)}\left[\frac{\alpha_o + c_R\lambda_b}{c_{S2}\lambda_a + \alpha_o - i\zeta_2} e^{\lambda_a z} - \frac{\alpha_o + \lambda_a c_R}{c_{S2}\lambda_b + \alpha_o - i\zeta_2} e^{\lambda_b z}\right] \tag{108}$$

The total solution for $S_2(z)$ is $S_2(z) = S_{2P}(z) + S_{2H}(z)$

$$S_2(z) = \frac{-i\kappa_2}{c_R(\lambda_a - \lambda_b)} \quad \frac{\alpha_o + c_R\lambda_b}{c_{S2}\lambda_a + \alpha_o - i\zeta_2} \quad e^{\lambda_a z} +$$

$$\frac{i\kappa_2}{c_R(\lambda_a - \lambda_b)} \quad \frac{\alpha_o + \lambda_a c_R}{c_{S2}\lambda_b + \alpha_o - i\zeta_2} \quad e^{\lambda_b z} + A_3 e^{\frac{-(\alpha_o - i\zeta_2)z}{c_{S2}}} . \qquad (109)$$

Use the boundary condition that $S_2(0) = 0$ to determine A_3.

$$0 = \frac{-i\kappa_2}{c_R(\lambda_a - \lambda_b)} \quad \frac{\alpha_o + c_R\lambda_b}{c_{S2}\lambda_a + \alpha_o - i\zeta_2} \quad +$$

$$\frac{i\kappa_2}{c_R(\lambda_a - \lambda_b)} \quad \frac{\alpha_o + \lambda_a c_R}{c_{S2}\lambda_b + \alpha_o - i\zeta_2} \quad + A_3 \qquad (110)$$

$$A_3 = \frac{i\kappa_2}{c_R(\lambda_a - \lambda_b)} \left[\frac{\alpha_o + c_R\lambda_b}{c_{S2}\lambda_a + \alpha_o - i\zeta_2} - \frac{\alpha_o + c_R\lambda_a}{c_{S2}\lambda_b + \alpha_o - i\zeta_2} \right] . \qquad (111)$$

The final expression for $S_2(z)$ is

$$S_2(z) \quad \frac{-i\kappa_2}{c_R(\lambda_a - \lambda_b)} \left\{ \frac{\alpha_o + c_R\lambda_b}{c_{S2}\lambda_a + \alpha_o - i\zeta_2} \quad e^{\lambda_a z} - \right.$$

$$\frac{\alpha_o + c_R\lambda_a}{c_{S2}\lambda_b + \alpha_o - i\zeta_2} \quad e^{\lambda_b z} - \left[\frac{\alpha_o + c_R\lambda_b}{c_{S2}\lambda_a + \alpha_o - i\zeta_2} \quad - \right.$$

$$\left. \left. \frac{\alpha_o + c_R\lambda_a}{c_{S2}\lambda_b + \alpha_o - i\zeta_2} \right] e^{\frac{-(\alpha_o - i\zeta_2)z}{c_{S2}}} \right\} . \qquad (112)$$

Note that the expression for S_1 is identical to Kogelnik's result for the amplitude of a singly diffracted wave, but that the S_2 result is different [10]. These results provide the quantitative basis for the statement made earlier that, under the Bragg condition for a given

grating vector, the diffraction is largely independent of the presence of other grating vectors, and the same is not true for scattering off the Bragg condition. Since Equations (65-67) are symmetric with respect to an interchange of subscripts 1 and 2, the situation opposite to what has just been described is realized if $\kappa_2 >> \kappa_1$, or when the coupling constants are comparable. This happens if the Bragg condition is fulfilled for $\vec{K}_2$. The solution for this situation is obtained from Equations (79), (89), (93), and (112) by interchanging subscripts 1 and 2.

The final case to consider is when the departure from the Bragg condition of the coupling constants and phases for the two grating vectors are comparable. Under these conditions, $\kappa_1 \approx \kappa_2$, $c_{S1} = c_{S2} = c_S$, and $\zeta_1 = \zeta_2 = \zeta$. Applying these conditions to Equations (65-67) yields

$$c_R R' + \alpha_o R = i(\kappa_1 + \kappa_2) S_i \tag{113}$$

$$c_S S_i' + (\alpha_o - i\zeta) S_i = i\kappa_i R \tag{114}$$

Rewriting Equation (114) gives

$$R = \frac{-ic_S}{\kappa_i} S_i' - i \frac{\alpha_o - i\zeta}{\kappa_i} S_i \cdot \tag{115}$$

Now substitute Equation (115) into Equation (113)

$$\frac{-ic_R c_S}{\kappa_i} S_i'' - ic_R \frac{\alpha_o - i\zeta}{\kappa_i} S_i' - \frac{i\alpha_o c_S}{\kappa_i} S_i' - i\alpha_o \frac{\alpha_o - i\zeta}{\kappa_i} S_i =$$

$$i(\kappa_1 + \kappa_2) S_i \cdot \tag{116}$$

$$\frac{ic_R c_S}{\kappa_i} S''_i + \frac{ic_R \alpha_o}{\kappa_i} S'_i + \frac{c_R \zeta}{\kappa_i} S'_i + \frac{i\alpha_o c_S}{\kappa_i} S'_i + \frac{i\alpha_o^2}{\kappa_i} S_i +$$

$$\frac{\alpha_o \zeta}{\kappa_i} S_i + i(\kappa_1 + \kappa_2) = 0 \tag{117}$$

$$(c_R c_S)S''_i + (c_R\alpha_o - ic_R\zeta + \alpha_o c_S) S'_i + (\zeta_o^2 - i\alpha_o\zeta + (\kappa_1+ \kappa_2)^2) S_i = 0 \tag{118}$$

Assume a solution of the form $S_i(z) = A_4 e^{\gamma z}$ and substitute into Equation (118).

$$\gamma^2 c_R c_S A_4 e^{\gamma z} + \gamma(c_R\alpha_o - c_R i\zeta + \alpha_o c_S) \; A_4 e^{\gamma z} + (\alpha_o^2 - \alpha_o i\zeta +$$

$$(\kappa_1 + \kappa_2)^2) \; A_4 e^{\gamma z} = 0 \tag{119}$$

$$\gamma^2 c_R c_S + \gamma(c_R\alpha_o - i\zeta c_R + \alpha_o c_S) + (\alpha_o^2 - i\zeta\alpha_o + (\kappa_1 + \kappa_2)^2) = 0 \tag{120}$$

The quadratic formula will give solution for γ.

$$\gamma = \frac{1}{2c_R c_S} \left\{ (-c_R\alpha_o + i\zeta c_R - \alpha_o c_S) \pm \left[(c_R\alpha_o - i\zeta c_R + \alpha_o c_S)^2 - \right. \right.$$

$$\left. \left. 4(c_R c_S)(\alpha_o^2 - i\zeta\alpha_o + (\kappa_1 + \kappa_2)^2 \right] \right]^{1/2} \Bigg\} \tag{121}$$

$$\gamma = \frac{1}{2c_R c_S} \left\{ - \alpha_o c_R + i\zeta c_R - \alpha_o c_S \pm \left[c_R^2\alpha_o^2 - \zeta^2 c_R^2 + \right. \right.$$

$$\alpha_o^2 c_S^2 - 2i\zeta c_R^2 \alpha_o - 2i\zeta\alpha_o c_R c_S + 2\alpha_o^2 c_R c_S - 4c_R c_S \alpha_o^2 +$$

$$\left. \left. 4i\zeta\alpha_o c_R c_S - 4c_R c_S(\kappa_1 + \kappa_2)^2 \right] \right]^{1/2} \Bigg\} \tag{122}$$

$$\gamma = \frac{1}{2c_R c_S} \left\{ -\alpha_o c_R + i\zeta c_R - \alpha_o c_S \pm \left[c_R^2\alpha_o^2 - \zeta^2 c_R^2 + \alpha_o^2 c_S^2 - \right. \right.$$

$$2i\zeta\alpha_o c_R^2 + 2i\zeta\alpha_o c_R c_S - 2\alpha_o^2 c_R c_S - 4c_R c_S(\kappa_1 + \kappa_2)^2\Big]^{1/2}\Bigg\} \tag{123}$$

$$\gamma = \frac{1}{2c_R c_S}\Bigg\{-\alpha_o c_R + i\zeta c_R - \alpha_o c_S \pm \Big[(c_R\alpha_o - c_S\alpha_o - i\zeta c_R)^2 - 4c_R c_S(\kappa_1 + \kappa_2)^2\Big]^{1/2}\Bigg\} \tag{124}$$

$$\bar{\gamma}a,b = (\tfrac{1}{2})\Bigg\{-\frac{\alpha_o}{c_S} + \frac{\alpha_o}{c_R} - i\frac{\zeta}{c_S} \pm \Big[(\frac{\alpha_o}{c_R} - \frac{\alpha_o}{c_S} - i\frac{\zeta}{c_S})^2 - \frac{4(\kappa_1 + \kappa_2)^2}{c_R c_S}\Big]^{1/2}\Bigg\} \tag{125}$$

Assume a solution for R of the form

$$R_{iz} = A_5 e^{\gamma_a z} + B_5 e^{\gamma_b z} \tag{126}$$

Using the boundary condition that R(0) = 1 and following the same procedure as done earlier in Equations (83-93) will give the result for $R_i(z)$.

$$R_{iz} = e^{\gamma_a z} + \frac{\alpha_o + \gamma_a c_R}{c_R(\gamma_a - \gamma_b)}\Big[e^{\gamma_b z} - e^{\gamma_a z}\Big] \tag{127}$$

The solution for $S_i(z)$ is made up of both a particular ($S_{iP}(z)$) and a homogeneous ($S_{iH}(z)$) solution. The method for obtaining the solution is the same as was done in Equations (94-112). Going through this procedure gives the following solution for $S_i(z)$,

$$S_i(z) = \frac{-i\kappa_i}{c_R(\gamma_a - \gamma_b)}\Bigg\{\frac{\alpha_o + c_R\gamma_b}{c_S\gamma_a + \alpha_o - i\zeta} e^{\gamma_a z} - \frac{\alpha_o + c_R\gamma_a}{c_S\gamma_b + \alpha_o - i\zeta} e^{\gamma_b z} - \Big[\frac{\alpha_o + c_R\gamma_b}{c_S\gamma_a + \alpha_o - i\zeta} -$$

$$\left.\left.\frac{\alpha_o + c_R\gamma_a}{c_S\gamma_b + \alpha_o - i\zeta}\right] e^{\frac{-(\alpha_o - i\zeta)z}{c_S}}\right\} \tag{128}$$

For comparison of these theoretical predictions with experimental results, some geometrical simplifications consistent with typical experimental situations can be imposed. Consider the first case treated above and let $\vec{K}_1$ and $\vec{K}_2$ lie along the same direction (e.g. the c-axis of a $LiNbO_3$ crystal) perpendicular to the normal as shown in Figure 1. Then $\phi_1 = \phi_2 = \frac{\pi}{2}$ and $c_R = c_{S1} = c_{S2} = \cos\theta$. Now introduce the dimensionless coupling constants

$$\nu_i = \frac{\kappa_i d}{\cos\theta} \quad , \quad (i = 1,2) \tag{129}$$

and the dimensionless dephasing parameters

$$\xi_i = \frac{\zeta_i d}{2\cos\theta} \quad , \quad (i = 1,2) \tag{130}$$

The expression in Equation (79) for $\lambda_{a,b}$ becomes

$$\lambda_{a,b} = \frac{1}{2}\left\{-\frac{\alpha_o}{\cos\theta} - \frac{\alpha_o}{\cos\theta} + i\,\frac{\zeta_i}{\cos\theta} \pm \left[\left(\frac{\alpha_o}{\cos\theta} - \frac{\alpha_o}{\cos\theta} - i\,\frac{\zeta_i}{\cos\theta}\right)^2 - \frac{4\kappa_i}{\cos^2\theta}\right]^{1/2}\right\} \tag{131}$$

$$\lambda_{a,b} = \frac{1}{2}\left\{-\frac{2\alpha_o}{\cos\theta} + i\,\frac{\zeta_i}{\cos\theta} \pm -\left[\frac{\zeta_i^2}{\cos^2\theta} - \frac{4\kappa_i^2}{\cos^2\theta}\right]^{1/2}\right. \tag{132}$$

$$\lambda_{a,b} = -\frac{\alpha_o}{\cos\theta} + i\,\frac{\zeta_i}{2\cos\theta} \pm \left[-\frac{\zeta_i^2}{4\cos^2\theta} - \frac{\nu_i^2}{d^2}\right]^{1/2} \tag{133}$$

The expression in Equation (89) for the amplitude of the primary curve at the exit surface using Equations (129), (130), and (133) becomes

$$S_1(d) = \frac{-i\nu_1\cos\theta}{d\cos\theta} \frac{e^{\left\{ -\frac{\alpha_o d}{\cos\theta} + i\frac{\zeta_1 d}{2\cos\theta} + \left[-\frac{\zeta_1^2 d^2}{4\cos^2\theta} - \nu_1^2 \right]^{1/2} \right\}} - e^{\left\{ -\frac{\alpha_o d}{\cos\theta} + i\frac{\zeta_1^2 d^2}{2\cos\theta} + \left[-\frac{\zeta_1^2}{4\cos^2\theta} - \frac{\nu_1^2}{d^2} \right]^{1/2} \right\}}}{e^{\left\{ -\frac{\alpha_o}{\cos\theta} + i\frac{\zeta_1}{2\cos\theta} + \left[-\frac{\zeta_1^2}{4\cos^2\theta} - \frac{\nu_1^2}{d^2} \right]^{1/2} \right\}} - e^{\left\{ -\frac{\alpha_o}{\cos\theta} + i\frac{\zeta_1}{2\cos\theta} - \left[-\frac{\zeta_1^2}{4\cos^2\theta} - \frac{\nu_1^2}{d^2} \right]^{1/2} \right\}}} \tag{134}$$

$$S_1(d) = i\nu_1 e^{\left[-\frac{\alpha_o d}{\cos\theta} + i\xi_1 \right]} \frac{e^{i(\xi_1^2 + \nu_1^2)^{1/2}} - e^{-i(\xi_1^2 + \nu_1^2)^{1/2}}}{\left[-\frac{\zeta_1^2 d^2}{4\cos^2\theta} - \nu_1^2 \right]^{1/2} + \left[-\frac{\zeta_1^2 d^2}{4\cos^2\theta} - \nu_1^2 \right]^{1/2}} \tag{135}$$

$$S_1(d) = \frac{-i\nu_1 e^{\left[-\frac{\alpha_o d}{\cos\theta} + i\xi_1 \right]} \left[2i\sin(\nu_1^2 + \xi_1^2)^{1/2} \right]}{2i\left[\nu_1^2 + \xi_1^2 \right]^{1/2}} \tag{136}$$

$$S_1(d) = -ie^{\left[-\frac{\alpha_o d}{\cos\theta} + i\xi_1 \right]} \frac{\sin(\nu_1^2 + \xi_1^2)^{1/2}}{\left[1 + \frac{\xi_1^2}{\nu_1^2} \right]^{1/2}} \tag{137}$$

The diffraction efficiency, as defined by Equation (64), is

$$\eta_1 = \frac{\nu_1^2}{(\xi_1^2 + \nu_1^2)} \; e^{\frac{-2\alpha_o d}{\cos\theta}} \; \sin^2(\nu_1^2 + \xi_1^2)^{1/2} \tag{138}$$

The same procedure can be followed for the second spot. The amplitude of the secondary wave at the exit surface can be rewritten as

$$S_2(d) = \frac{-i\nu_2}{d(\lambda_a - \lambda_b)} \left[B_6 e^{\lambda_a d} + A_6 e^{\lambda_b d} - (A_6 + B_6) e^{\frac{-(\alpha_o - i\zeta_2)d}{\cos\theta}} \right] \tag{139}$$

$$S_2(d) = \frac{1}{2} \left[\frac{\nu_2}{(\xi_1^2 + \nu_1^2)^{1/2}} \right] \left\{ A_6 e^{\left\{ -\frac{\alpha_o d}{\cos\theta} + i\frac{\zeta_1 d}{2\cos\theta} - \left[-\frac{\zeta_1^2 d^2}{4\cos^2\theta} - \right. \right.} \right.$$

$$\left. \left. - \nu_1^2 \right]^{1/2} \right\} + B_6 e^{\left\{ -\frac{\alpha_o d}{\cos\theta} + i\frac{\zeta_1 d}{2\cos\theta} + \left[-\frac{\zeta_1^2 d^2}{4\cos^2\theta} - \nu_1^2 \right]^{1/2} \right\}}$$

$$- (A_6 + B_6) e^{\left\{ -\frac{\alpha_o d}{\cos\theta} + i\frac{\zeta_2 d}{\cos\theta} \right\}} \Bigg\} \tag{140}$$

$$S_2(d) = \frac{1}{2} \left[\frac{\nu_2}{(\xi_1^2 + \nu_1^2)^{1/2}} \right] e^{-\frac{\alpha_o d}{\cos\theta}} \left\{ A_6 e^{\left[i\xi_1 - i(\xi_1^2 + \nu_1^2)^{1/2} \right]} + \right.$$

$$\left. B_6 e^{\left[i\xi_1 + i(\xi_1^2 + \nu_1^2)^{1/2} \right]} - (A_6 + B_6) e^{2i\xi_2} \right\} \tag{141}$$

where

$$A_6 = \frac{\alpha_o + c_R \lambda_a}{c_{S2}\lambda_b + \alpha_o - i\zeta_2} \tag{142}$$

and reduces to

$$A_6 = \frac{\alpha_o + \frac{\cos\theta}{2}\left\{-\frac{\alpha_o}{\cos\theta} - \frac{\alpha_o}{\cos\theta} + i\frac{\zeta_1}{\cos\theta} + \left[\left(\frac{\alpha_o}{\cos\theta} - \frac{\alpha_o}{\cos\theta} - i\frac{\zeta_1}{\cos\theta}\right)^2 - \right.\right.}{\frac{\cos}{2}\left\{-\frac{\alpha_o}{\cos\theta} - \frac{\alpha_o}{\cos\theta} + i\frac{\zeta_1}{\cos\theta} - \left[\left(\frac{\alpha_o}{\cos\theta} - \frac{\alpha_o}{\cos\theta} - \frac{i\zeta_1}{\cos\theta}\right)^2 - \right.\right.}$$

$$\left.\left.\left.\frac{4\kappa_1^2}{\cos^2\theta}\right]^{1/2}\right\}$$

$$\left.\left.\frac{4\kappa_1^2}{\cos^2\theta}\right]^{1/2}\right\} + \alpha_o - i\zeta_2 \qquad (143)$$

$$A_6 = \frac{\frac{i\zeta_1}{2} + \frac{1}{2}\left[-\zeta_1^2 - \frac{4\nu_1^2\cos^2\theta}{d^2}\right]^{1/2}}{\frac{i\zeta_1}{2} - \frac{1}{2}\left[-\zeta_1^2 - \frac{4\nu_1^2\cos^2\theta}{d^2}\right]^{1/2} - i\zeta_2} \qquad (144)$$

$$A_6 = \frac{i\xi_1 + (-\xi_1^2 - \nu_1^2)^{1/2}}{i\xi_1 - (-\xi_1^2 - \nu_1^2)^{1/2} - 2i\xi_2} \qquad (145)$$

$$A_6 = \frac{(\xi_1^2 + \nu_1^2)^{1/2} + \xi_1}{\xi_1 - 2\xi_2 - (\xi_1^2 + \nu_1^2)^{1/2}} \qquad (146)$$

and similarly for B_6

$$B_6 = \frac{-(\alpha_o + c_R\lambda_b)}{c_{S2}\lambda_a + \alpha_o - i\zeta_2} \qquad (147)$$

$$B_6 = \frac{-\left\{\alpha_o + \frac{\cos\theta}{2}\left\{-\frac{\alpha_o}{\cos\theta} - \frac{\alpha_o}{\cos\theta} + i\frac{\zeta_1}{\cos\theta}\left[\left(\frac{\alpha_o}{\cos\theta} - \frac{\alpha_o}{\cos\theta} - i\frac{\zeta_1}{\cos\theta}\right)^2 - \frac{4\kappa_1^2}{\cos^2\theta}\right]^{1/2}\right\}\right\}}{\frac{\cos\theta}{2}\left\{-\frac{\alpha_o}{\cos\theta} - \frac{\alpha_o}{\cos\theta} + i\frac{\zeta_1}{\cos\theta} + \left[\left(\frac{\alpha_o}{\cos\theta} - \frac{\alpha_o}{\cos\theta} - \frac{i\zeta_1}{\cos\theta}\right)^2 - \frac{4\kappa_1^2}{\cos^2\theta}\right]^{1/2}\right\} + \alpha_o - i\zeta_2} \quad (148)$$

$$B_6 = \frac{-\frac{i\zeta_1}{2} + \frac{1}{2}\left[-\zeta_1^2 - \frac{4\nu_1^2\cos^2\theta}{d^2}\right]^{1/2}}{\frac{i\zeta_1}{2} + \frac{1}{2}\left[-\zeta_1^2 - \frac{4\nu_1^2\cos^2\theta}{d^2}\right]^{1/2} - i\zeta_2} \quad (149)$$

$$B_6 = \frac{-i\xi_1 + (-\xi_1^2 - \nu_1^2)^{1/2}}{i\xi_1 - 2i\xi_2 + (-\xi_1^2 - \nu_1^2)^{1/2}} \quad (150)$$

$$B_6 = \frac{(\xi_1^2 + \nu_1^2)^{1/2} - \xi_1}{\xi_1 - 2\xi_2 + (\xi_1^2 + \nu_1^2)^{1/2}} \quad (151)$$

The diffraction efficiency for the second spot is

$$\eta_2 = \left[\frac{1}{4}\frac{\nu_2^2}{(\xi_1^2 + \nu_1^2)^{1/2}}\right] e^{-\frac{2\alpha_o d}{\cos\theta}} \left\{A_6 B_6 e^{\left[i\xi_1 - i(\xi_1^2 + \nu_1^2)^{1/2}\right.} - \right.$$

$$\left. i\xi_1 - i(\xi_1^2 + \nu_1^2)^{1/2}\right] + A_6 B_6 e^{\left[-i\xi_1 + i(\xi_1^2 + \nu_1^2)^{1/2}\right.} +$$

$$i\xi_1 + i(\xi_1^2 + \nu_1^2)^{1/2}\Big] + A_6(A_6 + B_6)e^{\left[i\xi_1 - i(\xi_1^2 + \nu_1^2)^{1/2} - 2i\xi_2\right]} +$$

$$A_6(A_6 + B_6)e^{\left[-i\xi_1 + i(\xi_1^2 + \nu_1^2)^{1/2} + 2i\xi_2\right]} - B_6(A_6 + B_6)e^{\left[i\xi_1 +\right.}$$

$$\left. i(\xi_1^2 + \nu_1^2)^{1/2} - 2i\xi_2\right] - B_6(A_6 + B_6)e^{\left[i\xi_1 + i(\xi_1^2 + \nu_1^2)^{1/2} - 2i\xi_2\right]} -$$

$$B_6(A_6 + B_6)e^{\left[-i\xi_1 + i(\xi_1^2 + \nu_1^2)^{1/2} + 2i\xi_2\right]}\Big\} \qquad (152)$$

$$\eta_2 = \frac{1}{4}\left[\frac{\nu_2^2}{\xi_1^2 + \nu_1^2}\right]e^{-\frac{2\alpha_o d}{\cos\theta}}\Big\{A_6B_6\Big[e^{2i(\xi_1^2 + \nu_1^2)^{1/2}} +$$

$$e^{-2i(\xi_1^2 + \nu_1^2)^{1/2}}\Big] - A_6(A_6 + B_6)\Big[e^{i(-\xi_1 + 2\xi_2 + (\xi_1^2 + \nu_1^2)^{1/2})} +$$

$$e^{-i(-\xi_1 + 2\xi_2 + (\xi_1^2 + \nu_1^2)^{1/2})}\Big] - B_6(A_6 + B_6)\Big[e^{i(-\xi_1 + 2\xi_2 -}$$

$$\left.(\xi_1^2 + \nu_1^2)^{1/2}) + e^{-i(-\xi_1 + 2\xi_2 - (\xi_1^2 + \nu_1^2)^{1/2})}\right]\Big\} \qquad (153)$$

$$\eta_2 = \frac{1}{2}\left[\frac{\nu_2^2}{\xi_1^2 + \nu_1^2}\right]e^{-\frac{2\alpha_o d}{\cos\theta}}\Big\{A_6B_6\cos^2(\xi_1^2 + \nu_1^2) -$$

$$A_6(A_6 + B_6)\cos^2\left[\frac{2\xi_2 - \xi_1 - (\xi_1^2 + \nu_1^2)^{1/2}}{2}\right] -$$

$$B_6(A_6 + B_6)\cos^2\left[\frac{2\xi_2 - \xi_1 + (\xi_1^2 + \nu_1^2)^{1/2}}{2}\right]\Bigg\} \qquad (154)$$

which can be rewritten as

$$\eta_2 = \frac{1}{2}\left[\frac{\nu_2^2}{\xi_1^2 + \nu_1^2}\right] e^{-\frac{2\alpha_o d}{\cos\theta}}\Bigg\{A_6(A_6 + B_6)\sin^2\left[\frac{2\xi_2 - \xi_1 - (\xi_1^2 + \nu_1^2)^{1/2}}{2}\right] +$$

$$B_6(A_6 + B_6)\sin^2\left[\frac{2\xi_2 - \xi_1 + (\xi_1^2 + \nu_1^2)^{1/2}}{2}\right] - A_6B_6\sin^2(\xi_1^2 + \nu_1^2)^{1/2}\Bigg\} \; . \qquad (155)$$

At the exact Bragg condition for $\vec{K}_1$ or when $\xi_1 << \nu_1$, Equation (154) is reduced as follows

$$\eta_2 = \frac{1}{2}\left[\frac{\nu_2^2}{\nu_1^2}\right] e^{-\frac{2\alpha_o d}{\cos\theta}}\Bigg\{A'(A' + B')\sin^2\left[\frac{2\xi_2 - \nu_1}{2}\right] +$$

$$B'(A' + B')\sin^2\left[\frac{2\xi_2 + \nu_1}{2}\right] - A'B'\sin^2(\nu_1)\Bigg\} \qquad (156)$$

where

$$A' = \frac{\nu_1}{2\xi_2 + \nu_1} \qquad (157)$$

$$B' = \frac{\nu_1}{2\xi_2 - \nu_1} \qquad (158)$$

Now substitute in and reduce

$$\eta_2 = \frac{1}{2}\left[\frac{\nu_2^2}{\nu_1^2}\right] e^{-\frac{2\alpha_o d}{\cos\theta}} \left\{ \frac{\nu_1}{2\xi_2 - \nu_1} \quad \frac{4\xi_2 \nu_1}{4\xi_2^2 - \nu_1^2} \sin^2\left[\frac{2\xi_2 - \nu_1}{2}\right] + \right.$$

$$\left. \frac{\nu_1}{2\xi_2 + \nu_1} \quad \frac{4\xi_2\nu_1}{4\xi_2^2 - \nu_1^2}\left[\sin^2 \quad \frac{2\xi_2 + \nu_1}{2}\right] - \quad \frac{\nu_1^2}{4\xi_2^2 - \nu_1^2} \quad \sin^2(\nu_1)\right\} \tag{159}$$

$$\eta_2 = \frac{1}{2}\left[\frac{\nu_2^2}{4\xi_2^2 - \nu_1^2}\right] e^{-\frac{2\alpha_o d}{\cos\theta}} \left\{ \frac{4\xi_2}{2\xi_2 - \nu_1} \sin^2\left[\frac{2\xi_2 - \nu_1}{2}\right] + \right.$$

$$\left. \frac{4\xi_2}{2\xi_2 + \nu_1} \quad \sin^2\left[\frac{2\xi_2 + \nu_1}{2}\right] - \sin^2(\nu_1)\right\} \tag{160}$$

CHAPTER III

COMPUTER SIMULATIONS

Properties of Lossless Phase Gratings

In this section, properties of lossless phase gratings predicted by the theory are described. Most of the conclusions drawn from this analysis can be applied to amplitude grating having purely imaginary coupling constants κ_i and for combined amplitude and phase gratings where the coupling constants are complex numbers. For a phase grating, the coupling constants defined by Equation (20) have only a real part,

$$\kappa_i = \frac{\pi \Delta n_i}{\lambda} \quad \text{and} \quad \alpha = \Delta\alpha_i = 0. \tag{161}$$

The depth of modulation of the index of refraction Δn varies sinusoidally in a direction perpendicular to the z axis. This produces a nonuniform modulation of the phases of the electric field of the probe beam. The modulation is in a direction perpendicular to the z axis causing diffraction to occur.

Figures 2 and 3 are different angular diffraction profiles for the first spot under a variety of conditions which are relevant to experimental studies of $LiNbO_3$. These patterns are for the case of unslanted gratings close to the Bragg condition where the scattering is dominated by a single spatial frequency component of the grating. A Bragg angle of $\theta_B = 3^o$ is assumed and the computer simulated diffraction

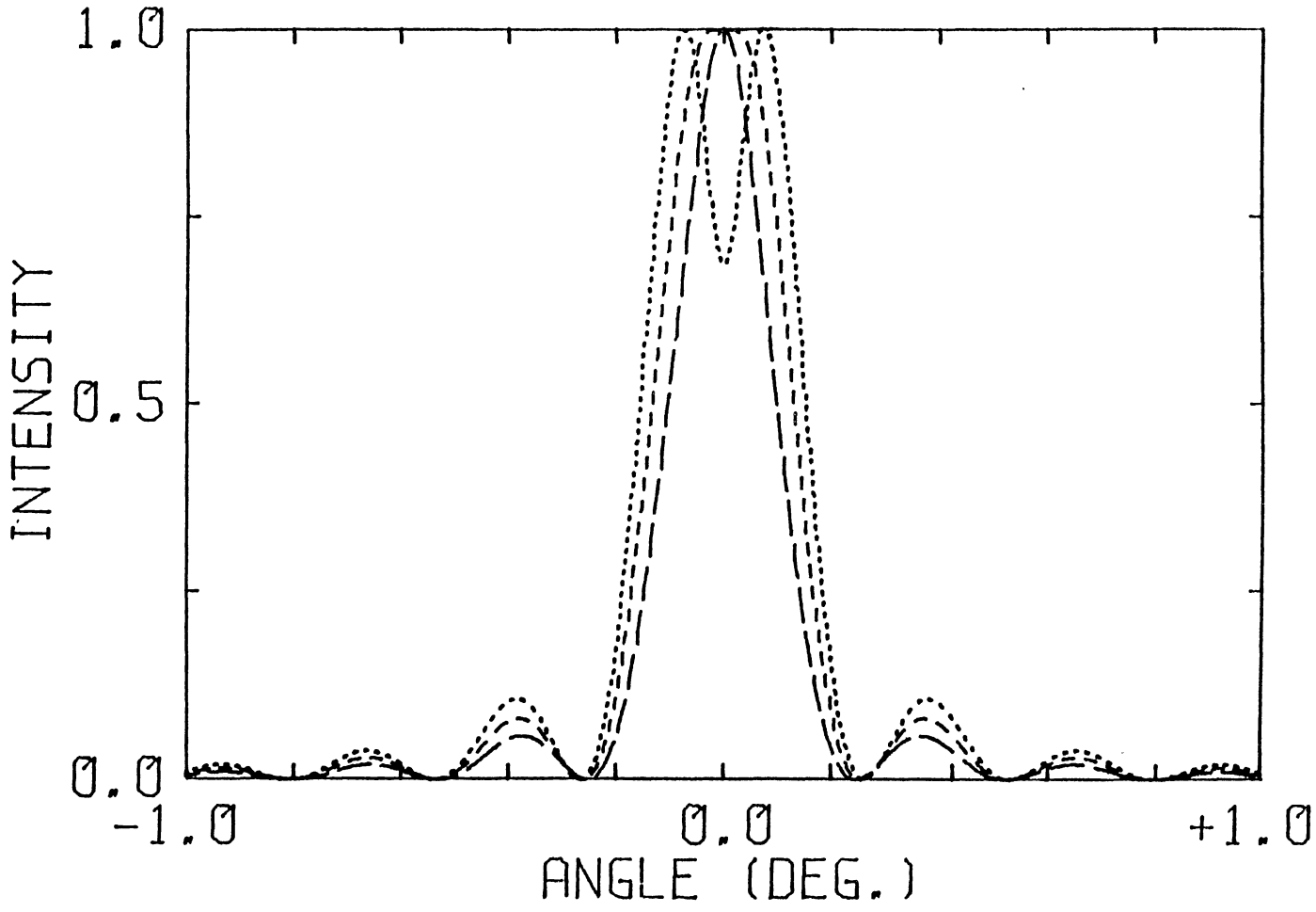

Figure 2. Computer Simulated Small Angle Scattering Patterns for $\theta_B = 3^o$ and d = 400 μm. The Broad Dashed Line is for $\Delta n = 4 \times 10^{-4}$; the Short Dashed Line for $\Delta n = 3 \times 10^{-4}$; and the Dotted Line for $\Delta n = 2 \times 10^{-4}$

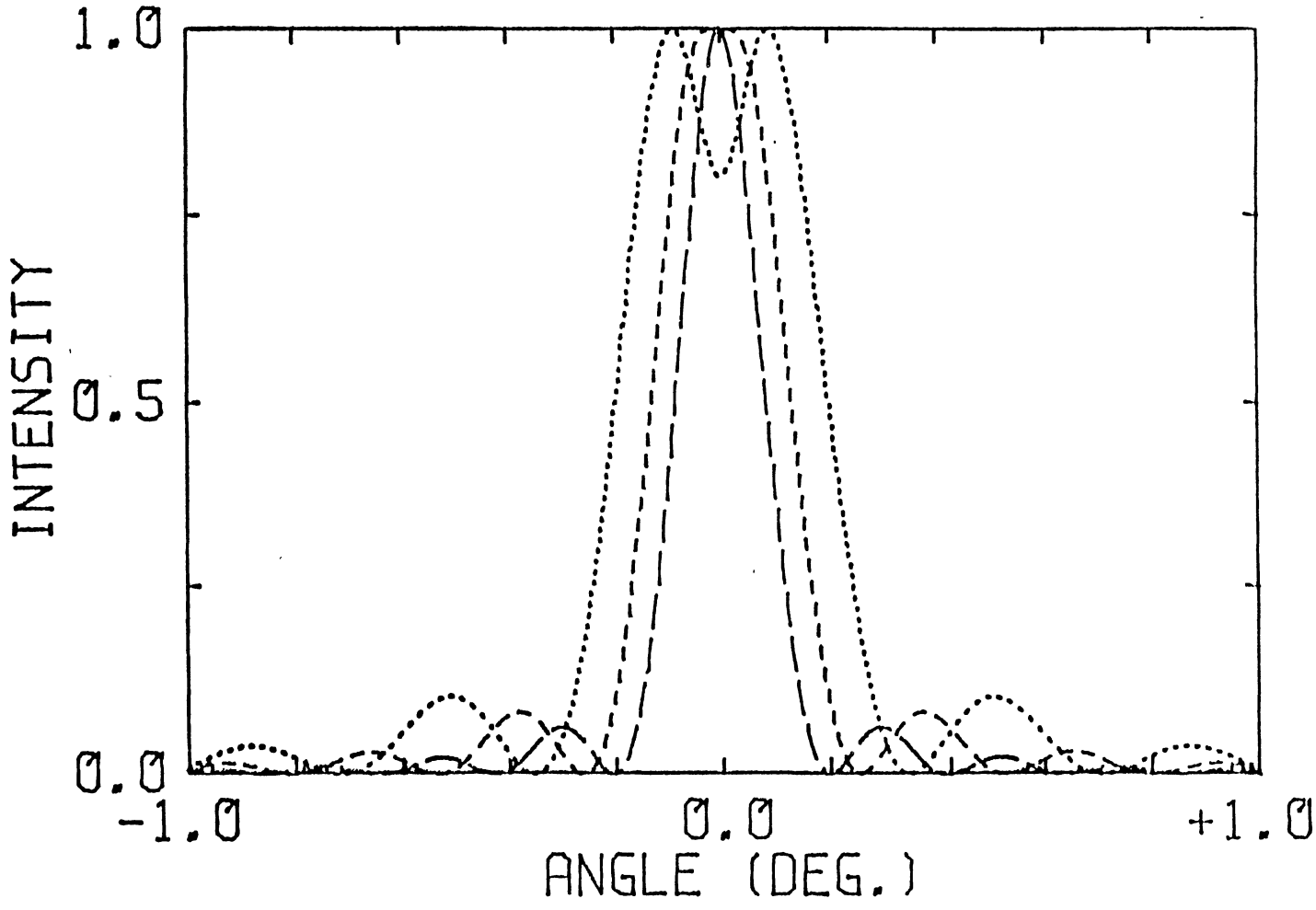

Figure 3. Computer Simulated Small Angle Scattering Patterns for $\theta_B = 3^o$ and $\Delta n = 3 \times 10^{-4}$. The Broad Dashed Line is for d = 500 μm; the Short Dashed Line for d = 400 μm; and the Dotted Line for d = 300 μm

patterns between $\pm 1^{o}$ of the Bragg angle are generated by Equation (138). The diffraction patterns are normalized to a peak intensity of 1.0.

In Figure 2 the grating thickness is fixed at 400 μm while the modulation depth is varied between 2×10^{-4} and 4×10^{-4}. The diffraction patterns all have a pronounced central peak with side lobes on both wings. The shape of this central peak is very sensitive to changes in Δn and change as the product of Δn and d, the grating thickness. For a deep grating (long write time, large write angle), the central peak is very sharp. For a shallow grating (short write time, small write angle), the diffraction pattern exhibits a broad, split central peak. The splitting of the diffraction pattern which causes the maximum scattering to occur off Bragg condition is a real physical effect [11] and not a theoretical artifact of the computer generated pattern. Also, for a given grating thickness, the angular separation of the side lobes is constant while their amplitudes decrease with an increase in grating depth.

In Figure 3, scattering profiles generated for a fixed grating depth of $\Delta n = 3 \times 10^{-4}$ and grating thicknesses of 300 μm, 400 μm, and 500 μm are shown. As in Figure 2, the width and shape of the pronounced central peak change with changes in d and vary as the produce on Δn and d. For thick gratings the central peak is sharp while thin gratings produce a broad, split central peak. In addition, both the amplitude and angular separation of the side lobes are strongly dependent upon the grating thickness. As the thickness of the grating decreases, the frequency of the side lobe decreases and the amplitude of the side lobes increases.

The computer generated diffraction patterns show that as gratings become deeper or thicker, the intensity of the scattered wave becomes concentrated in a well defined region at the Bragg angle. In the limit of an infinitely thick or infinitely deep grating, the scattering pattern has the form of a delta function in the direction satisfying the Bragg phase matching condition. For most real experimental situations, laser-induced gratings will produce scattering patterns with a significant amount of intensity at angles slightly varying form Θ_B.

Uncollimated Beams

The probe and signal beams are never perfectly collimated. This section determines how the signal seen by a detector with a small acceptance angle compares to that predicted for perfect Bragg scattering. Figures 4 and 5 show this comparison as a function of grating depth and grating thickness, respectively. At the Bragg angle, the scattering efficiency is found from Equation (138) to be

$$\eta_B = \exp\left[\frac{2\alpha_o d}{\cos\Theta_B}\right] \sin^2\left[\frac{\pi\Delta n d}{(\lambda\cos\Theta_B)}\right] . \tag{162}$$

The scattering efficiency averaged over a small angle $\Delta\Theta$ around the Bragg angle is

$$\langle\eta\rangle = \int_{\Theta_B - \Delta\Theta}^{\Theta_B + \Delta\Theta} \eta(\Theta') \frac{d\Theta'}{(2\Delta\Theta)} \tag{163}$$

where $\eta(\Theta')$ is given by Equation (138). The curves in the figure were generated for $\Delta\Theta = \pm 0.025^o$ and a Bragg angle of 3^o.

Figure 4 compares the dependence of scattering efficiency on grating modulation depth with a grating thickness of 400 μm for a well collimated probe beam versus a slightly converging or diverging beam. For very deep gratings, an oscillatory dependence appears for both collimater and averaged scattering efficiencies due to the interference effect of the phase modulated signal contributions scattered from different parts of the grating. At smaller modulation depths, the curve for the collimated signal obeys the simple relationship

$$\eta_B \alpha |\Delta n|^2 d^2. \tag{164}$$

This relationship is frequently used in describing the results of laser induced grating experiments. The deviation from the quadratic dependence occurs above a scattering efficiency of 90%. This indicates that the validity of Equation (164) is not limited to small angles of η_B.

For large values of Δn, the curve for the averaged scattering efficiency closely follows the curve for η_B. This is not surprising since for deep gratings most of the light is scattered in the Bragg direction leading to

$$\eta_B \approx \langle \eta \rangle . \tag{165}$$

However, at small values of Δn, $\langle \eta \rangle$ departs from the quadratic dependence predicted by Equation (164) due to the splitting of the central peak as seen in the diffraction patterns. Averaging the signal over small angles around the Bragg peak includes more of the scattered light intensity than seen at the exact Bragg angle leading to

$$\langle \eta \rangle >> \eta_B. \tag{166}$$

The curve in Figure 4 tends toward a constant value of $\langle \eta \rangle$ for small

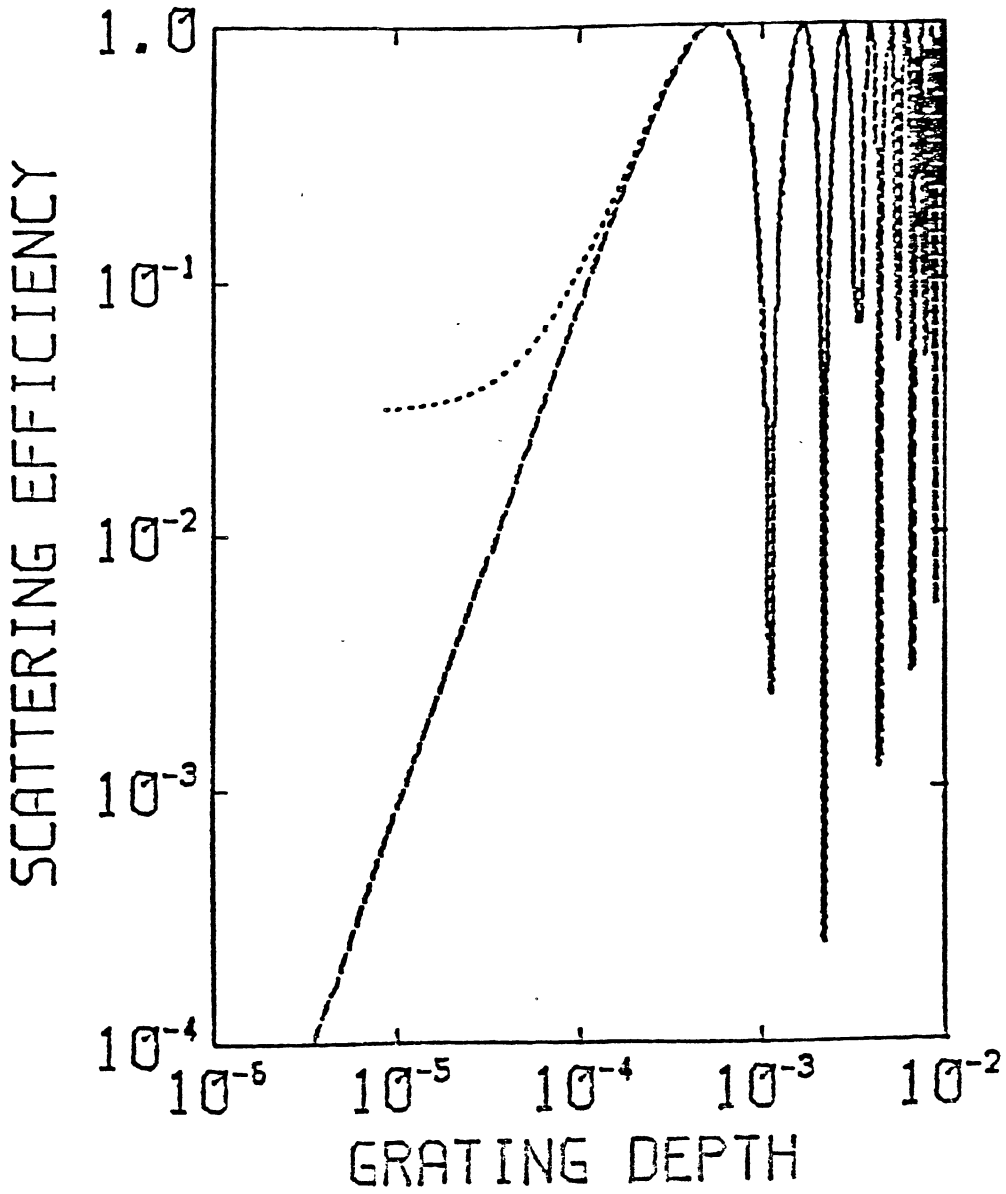

Figure 4. Computer Simulated Scattering Efficiency as a Function of Grating Depth, Δn, for $\theta_B = 3^o$ and d = 400 μm. The Broken Line is for Exact Bragg Scattering While the Dotted Line is the Average Value $\pm 0.025^o$ about θ_B

Δn. Although the deviation from a quadratic dependence is real, the exact dependence shown is unphysical and due to the simplifications made in deriving Equations (49-52) in which the second derivatives of the fields R" and S_i'' were neglected compared to the coupling constant κ_i.

Figure 5 compares the dependence of scattering efficiency on grating thickness for a grating of depth $\Delta n = 1.0 \times 10^{-4}$ for a well collimated probe beam versus a slightly diverging or converging beam. The angular average is again taken for $\Delta\theta = \pm 0.025^{\circ}$ around $\theta_B = 3^{\circ}$. For very thick gratings both η_B and $\langle\eta\rangle$ show an oscillatory behavior due to interference effects of light scattered from different parts of the grating. For thin gratings both η_B and $\langle\eta\rangle$ vary quadratically with d as predicted by Equation (163). The magnitude for the angular average scattering efficiency is greater than the exact Bragg scattering efficiency due to the splitting of the central peak. The smaller the value of d, the greater the range of Δn for which Equation (164) will be valid.

Restrictions of Expression for Computer Simulations

The above discussion of computer simulated scattering results shows that the simple expression given in Equation (164) which is generally used to interpret scattering data from laser-induced gratings is valid only for very restricted conditions. One condition is having a simple sinusoidal grating which is produced only if the laser beams writing the grating are exactly collimated beams with uniform intensity throughout the region to be probed and if the charge relocation dynamics are simple

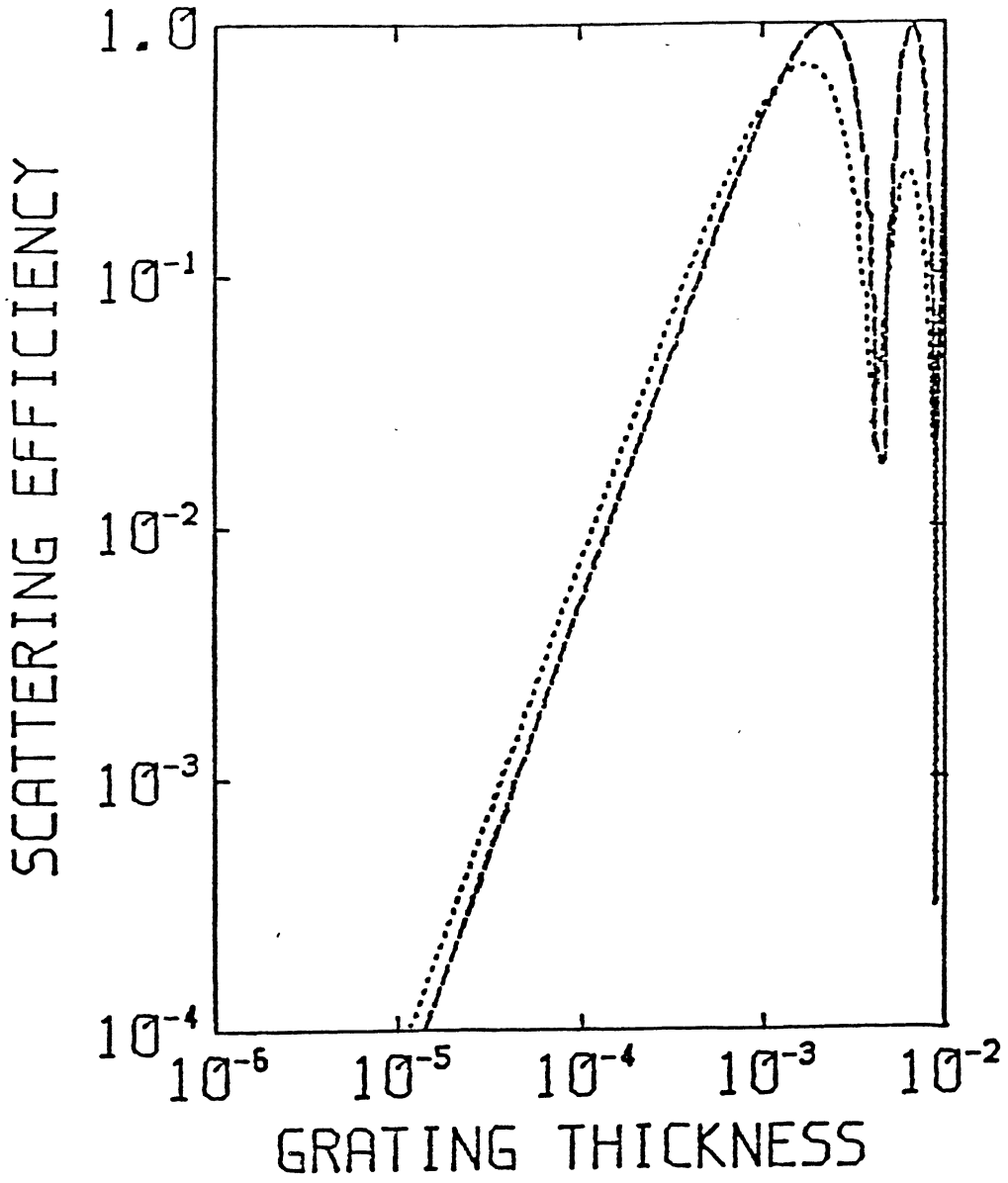

Figure 5. Computer Simulated Scattering Efficiency as a Function of Grating Thickness, d, for $\theta_B = 3^\circ$ and $\Delta n = 1 \times 10^{-4}$. The Broken Line is for Exact Bragg Scattering While the Dotted Line is the Average Value $\pm$ 0.025° about θ_B

enough to replicate the shape of the laser interference pattern. Another condition is having the modulation depth and thickness large enough to have most of the scattered light concentrated in the central Bragg peak but not so large that interference effects occur from light scattered from different parts of the grating. The probe and signal beams must also be well collimated so that the detector only sees light scattered at the exact Bragg condition.

Keeping in mind the above restrictions, angular scattering patterns can be fitted. Fitting these curves is a method for obtaining accurate values for the grating depth and grating thickness. The accuracy of these values cannot be obtained from the results of Bragg scattering efficiency measurements. In the following sections experimentally measured scattering patterns are reported and compared to these theoretically predicted patterns in order to determine the physical properties of the gratings.

CHAPTER IV

EXPERIMENTAL PROCEDURE

Samples

Four sets of samples were analyzed using the technique described earlier. The first set of samples consisted of good optical quality single crystals of poled $LiNbO_3$. This was "nominally pure" material obtained commercially and contained a total concentration of transition metal ion impurities of between 25 and 50 ppm.

The second set of samples consists of four crystals of poled $LiNbO_3$ obtained from Union Carbide. These four crystals contained different amounts of magnesium doping. The mole percentages of magnesium doping was at 1.8%, 3.6%, 5.0%, and 8.8%. The first three crystals were stoichiometric melt and the 8.8% crystals was congruent melt.

The third set of samples consists of four good optical quality single crystals of poled $LiNbO_3$ that have been chemically diffused with protons. Each sample was soaked in benzoic acid at 240^{o}C in a sealed tube for a varying amount of time. This is a standard technique of proton exchange. Benzoic acid has been shown to have an appropriate dissociation constant, melting temperature, and stability as a liquid for use in this process [12]. Sample #1 was soaked for 2 days, sample #2 for 4 days, sample #3 for 8 days, and sample #4 for 14 days. Each of the four crystals was annealed at 400^{o}C for six days in sealed tubes.

The tubes were then opened exposing the samples to the atmosphere and they were again annealed at 400^{o}C for nine more days. Annealing converts the step index profile obtained with photon exchange to a gradiant-index profile having a lowered value of Δn at the guide surface [13]. Post-annealing also controls the crystal phase of the exchange layer and stabilize the surface index [12].

The fourth set of samples consists of two doped crystals of $LiNbO_3$. The first was $LiNbO_3:Cu^{2+}$. In this crystal there was 1% doping of Cu in $LiNbO_3$. The second crystal was $LiNbO_3$:Er with approximately 0.05% Erbium.

Absorption Spectra

The absorption spectral of the five samples probes is shown in Figure 6. Neither the 442 nm write beam nor the 632 nm probe beam lies on a sharp absorption band. The nominally pure absorption band and the proton diffused absorption band are similar. The absorption coefficient is approximately the same at the wavelength of the write and probe beams. This can also be said for $LiNbO_3$:Er and $LiNbO_3$:Mg. In the $LiNbO_3:Cu^{2+}$ absorption band, the absorption coefficient at the wavelength of the write beam is almost four times greater than at the wavelength of the probe beam.

Apparatus

Photorefractive gratings were established and probed using the experimental setup shown as a block diagram in Figure 7. The 442 nm emission from a 16 mW He-Cd laser was used to write and erase the photo-refractive holograms. The 632 nm emission from a 6 mW He-Ne laser

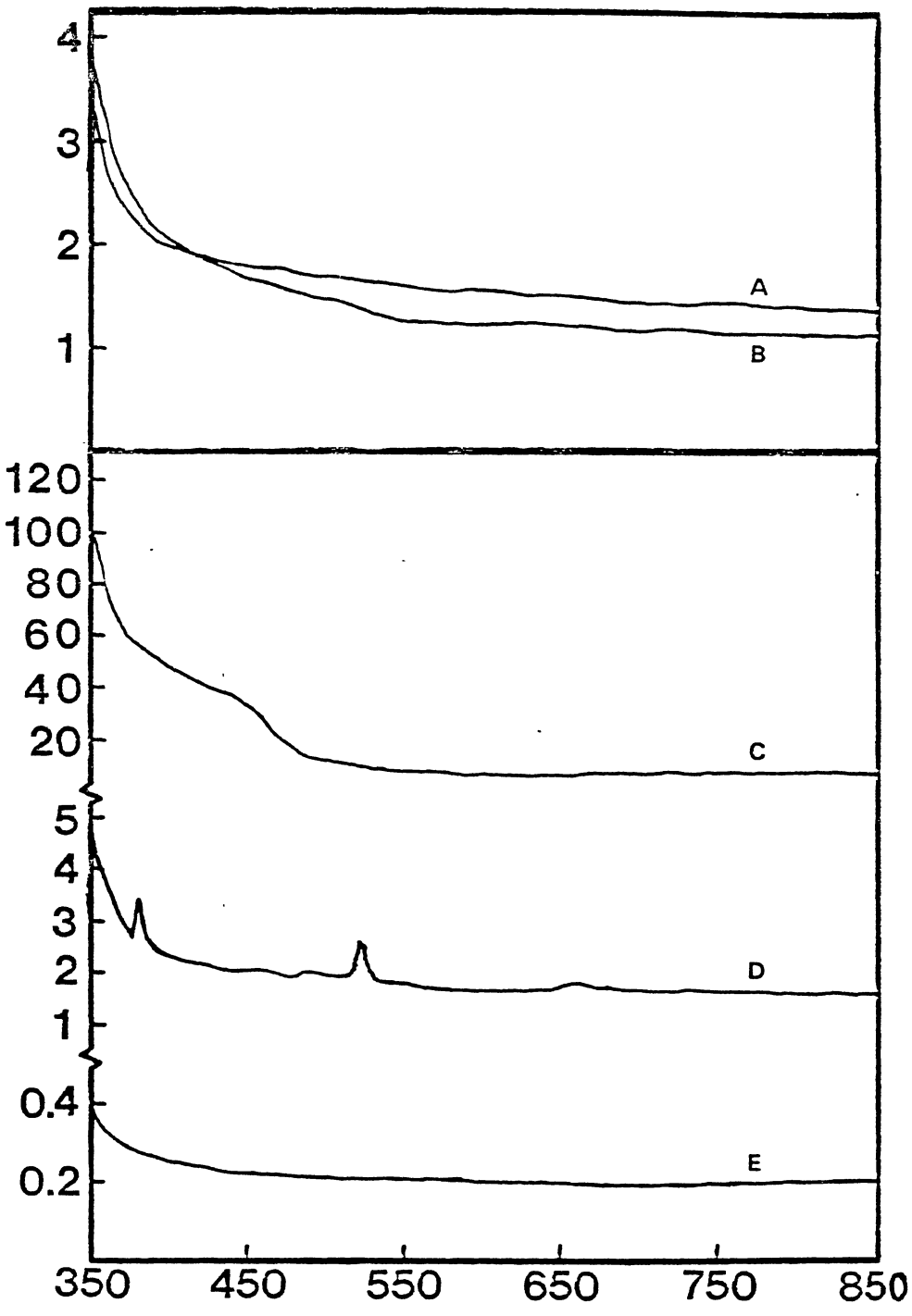

Figure 6. Absorption Spectra of Doped Samples of $LiNbO_3$. (A) Proton Diffused $LiNbO_3$; (B) Nominally Pure $LiNbO_3$; (C) Copper Doped $LiNbO_3$; (D) Erbium Doped $LiNbO_3$; (E) Magnesium Doped $LiNbO_3$

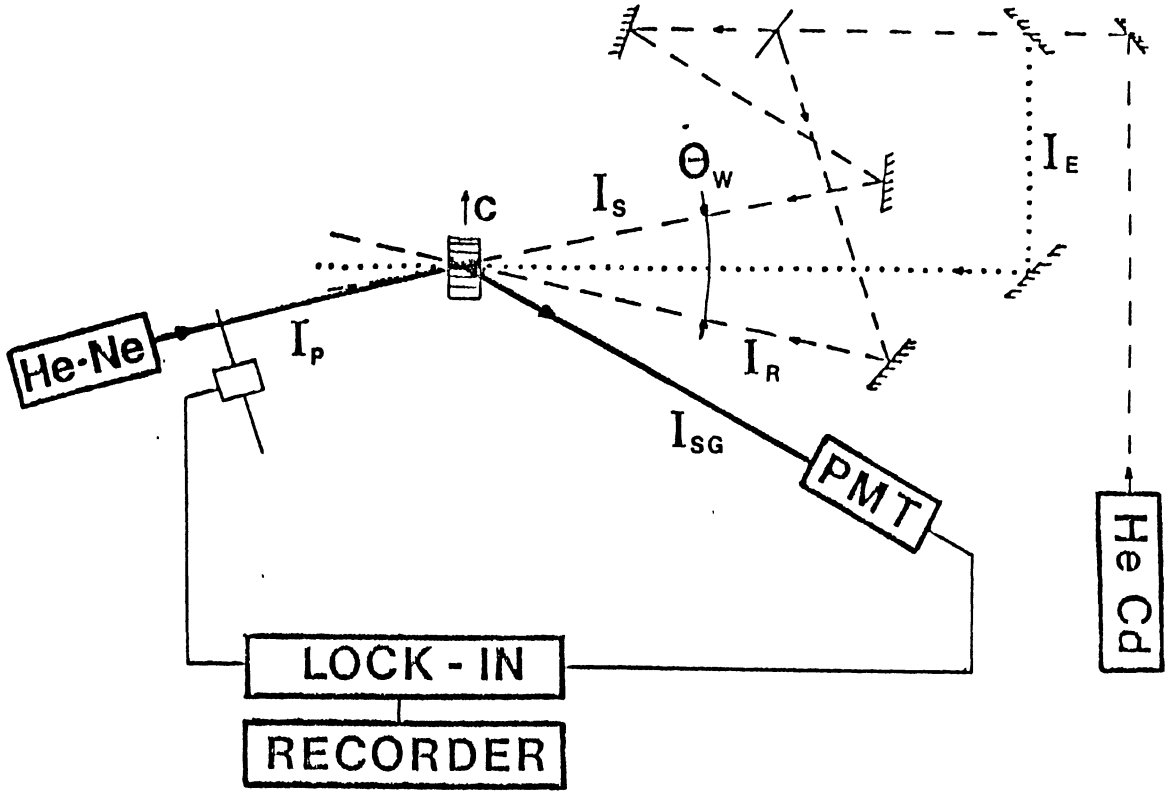

Figure 7. Block Diagram of the Experimental Setup. He-Cd and He-Ne are the Lasers Used to Write (and Erase) and Probe the Gratings, Respectively

was used to probe the grating without damaging the hologram. The scattered signal beam was chopped and then detected by an RCA C31034 photomultiplier tube and recorded with the help of a lock-in amplifier to improve the signal to noise ratio.

In these experiments, the write beam was split into two components with the use of a beam splitter. These two components were then superimposed inside the sample producing an interference pattern in the shape of a grating. The charge relocation associated with the PRE in the peak regions of the grating reached steady state conditions in 20 seconds to 15 minutes. The time for steady state conditions depends upon dopings and characteristics of the crystal used. The properties of the resulting holographic grating were investigated by monitoring the scattering efficiency of the probe beam as a function of scattering angle. This was accomplished by slight rotations of the base on which the sample was mounted which is equivalent to varying the angles of the probe and signal beams with respect to the induced grating. The details of this geometry are shown in Figure 7.

The phase grating developes in $LiNbO_3$ because of the interference pattern of the two write beams. The phase grating originates from charges that have become detrapped and migrate because of drift, diffusion, and the bulk photovoltaic effect. The transportation of charge causes a periodic electrostatic field to develop inside the crystal. The electrostatic field in turn causes a modulation of the index of refraction of the material. The final shape of the refractive grating index can be different from the sinusoidal interference pattern of the crossed laser beams.

The above technique was used on the four sets of samples and a grating thickness and modulation depth was determined using the computer fit described earlier. For the first set of samples, write beam crossing angles of 2.5°, 4.0°, and 8.0° were used. For the other sample sets a write angle of 4° was used. Different write times will give different values for a grating thickness and grating depth. The scattering pattern is very dependent upon the write time. If the write time is too long or too short, then Equation (138) does not provide a good fit for the data. The write time was varied from 20 seconds to 15 minutes for the first set of samples. For the second and third sample sets a write time of 2 minutes proved to provide the best pattern. A write time of 30 seconds was used on the third set of samples. The scattering pattern each sample was fitted with the computer.

In the "nominally pure" crystal of $LiNbO_3$, the erasure of the hologram was monitored and compared with the scattering properties for honograms with different grating spacings. Erasure was accomplished by inserting the movable mirror into the path of the HeCd laser beam as shown in Figure 7. The uniform illumination of the sample with the HeCd laser beam relocates the trapped charges in a random distribution. This uniform illumination therefore "erases" the photorefractive grating hologram. The grating was created with a one minute write time and then partially erased. The scattering properties of the hologram are then recorded and erasure was continued. To avoid problems with partially erased gratings in the other samples, the samples were thermally annealed in air at $500^{\circ}C$ for one hour after each measurement of the diffraction pattern.

CHAPTER V

EXPERIMENTAL RESULTS AND DISCUSSION

Introduction

As presented earlier, the main scope of this study is to develop and apply an expression for the angular distributions of the scattering pattern. The grating which produces this diffraction pattern is a complex grating having multiple Fourier components. From the expression developed, information concerning the refractive index modulation of each component of the grating can be obtained. The results of this technique are given in the following sections.

Results for "Nominally Pure" $LiNbO_3$

The results presented here were obtained from "nominally pure" crystals of $LiNbO_3$. The diffraction pattern that developed in $LiNbO_3$ was observed to consist of three primary maxima. The scattering pattern of the three primary maxima for a write angle of 4.5^o is shown in Figure 8. The direction of these three diffracted beams show that they originate from different spacial frequencies of the write beams' interference pattern. These different spacial frequencies contributing to the refractive index grating consist of the fundamental, first, and second harmonics of the write beams' interference pattern. The presence of the harmonic frequencies is caused by the nonlinearities in the charge

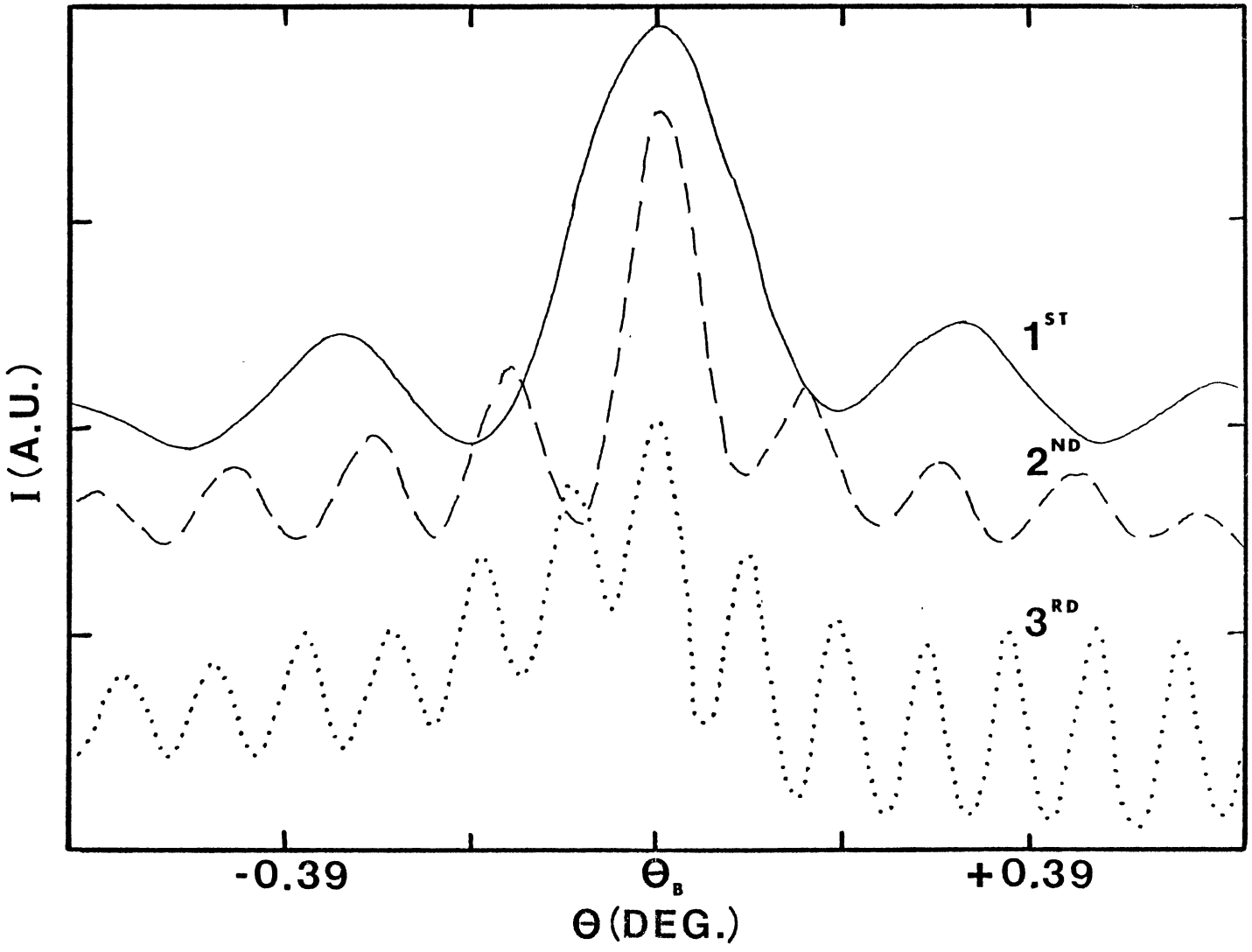

Figure 8. Scattering Pattern of the Three Primary Maxima for a Write Angle of 4.5° in "Nominally Pure" $LiNbO_3$

transport of the ions. The charge transport is induced by the interaction between the light interference pattern and the space charge field which is built up by the charge relocation. Different frequency components of the grating were observed to have different erasure times. This was observed by measuring the different time dependences of the three scattering maxima under uniform illumination of the sample causing grating erasure. Different erasure times are shown in Figure 9. The rate of decay of the Fourier component is different for each component and increases as you increase the order of the spot (whether it be 1st, 2nd, or 3rd). The decay rates of each spot is shown in Figure 9 for a grating formed at a write angle of 4.2^{o}.

Figure 10 shows examples of the small angle scattering patterns around the three primary scattering maxima measure on $LiNbO_3$ at a write beam crossing angle of 2.5^{o} and a write time of 2 minute. Computer fits to the observed data were obtained from Equation (138) treating the grating modulation depth and thickness as adjustable parameters. A good fit is obtained from the scattering pattern associated with the fundamental grating frequency as shown in Figure 10.(A). This was obtained for values of $\Delta n_1 = 3.48 \times 10^{-4}$ and $d_1 = 370$ μm and is extremely sensitive to the choice of both parameters. It was determined that it is best to adjust the thickness parameter until the frequency of the side bands were equal, and then to adjust the grating depth until the full width half maximum of the central peak was the same. These values were used as initial parameters for the fitting routine. The fit between theory and experiment is poorer for the pattern associated with the 1st harmonic of the laser interference pattern as shown in Figure 10(B).

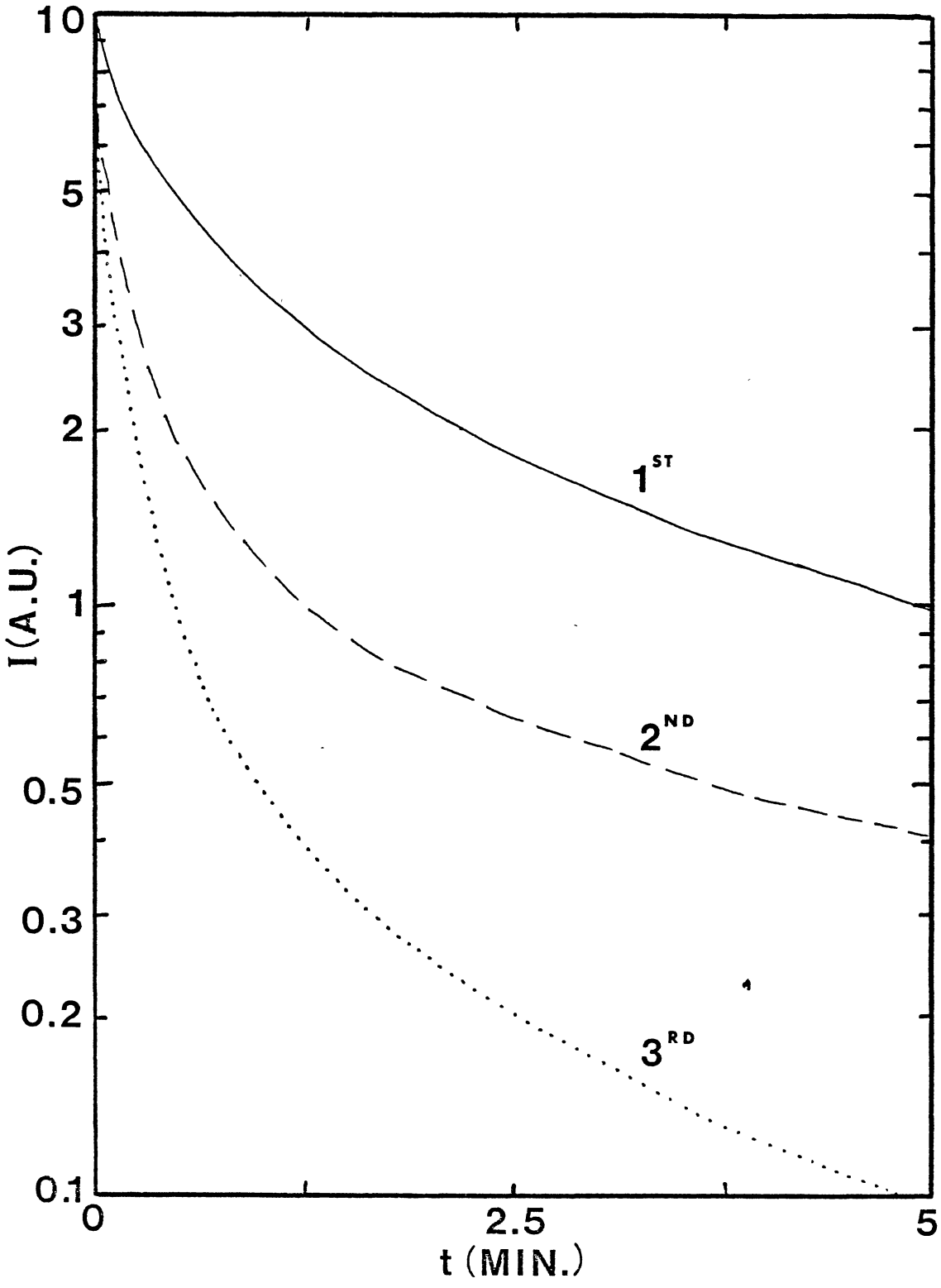

Figure 9. Decay of the Three Primary Maxima for a Grating Formed at a Write Angle of 4.2° in "Nominally Pure" $LiNbO_3$

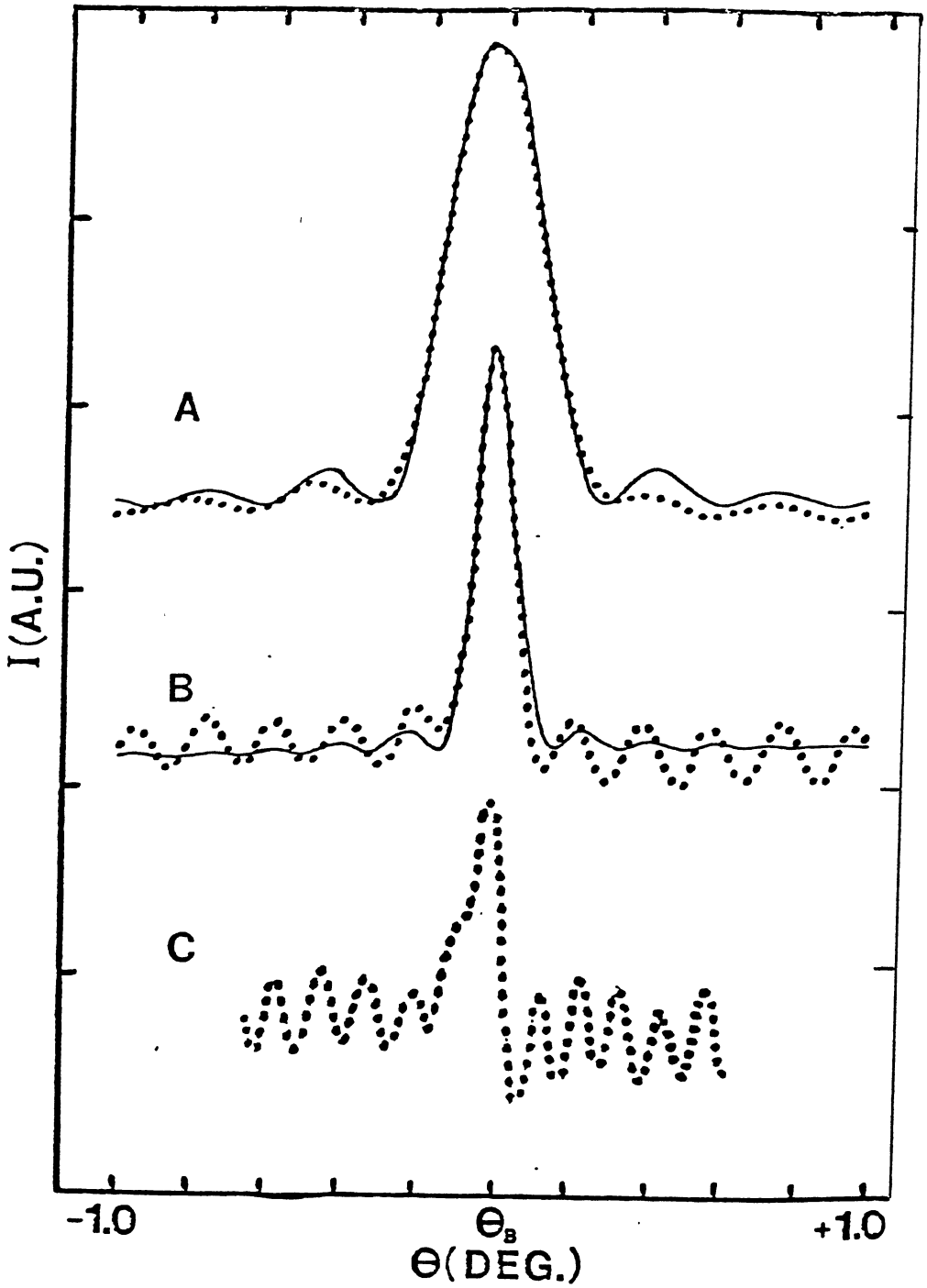

Figure 10. Small Angle Scattering Patterns Around the Three Scattering Maxima for $LiNbO_3$ After a 2 Min Write Time at $\Theta_W = 2.5^o$. The Dotted Lines are the Experimental Measurements and the Solid Lines are Computer Simulated Fits to the Data. (A) First Spot $\Theta_B = 2.8^o$; d = 370 μm; $\Delta n = 3.48 \times 10^{-4}$; (B) Second Spot $\Theta_B = 4.69^o$; d = 401 μm; $\Delta n = 4.62 \times 10^{-4}$; (C) Third Spot $\Theta_B = 6.3^o$

However, the best fit gives estimates for the depth and thickness of this component of the grating as $\Delta n_2 = 4.62 \times 10^{-4}$ and $d_2 = 401$ μm. The scattering from the grating component associated with the second harmonic of the laser interference pattern shown in Figure 10(C) has a very asymetric central peak and therefore cannot be described by Equation (138).

The results of comparing experimentally observed scattering patterns with computer generated patterns for multi-Fourier component gratings as shown in Figure 10 demonstrate that the assumptions underlying the derivation of Equation (138) are valid for scattering from the fundamental grating component but become less valid for scattering from progressively higher order frequencies of the grating. This is due to the fact that the nonlinear interaction between the migrating charges and the induced space charge field is greater for higher spacial frequencies. The nonlinear interaction results in a greater departure from a sinusoidal grating shape which breaks down the assumption that the probe and scattered waves couple through a single frequency of the Fourier series of the refractive index grating. The experimentally observed pattern shown in Figure 10(c) has large phase correlated contributions associated with scattering from different spacial frequencies of the grating. These show up as large oscillations in the wings of the scattering pattern with nondecaying amplitudes. This type of pattern is predicted in the theory by Equation (154). Equation (154) describes the case of a grating with two spacial frequencies probed off Bragg conditions and with comparable coupling constants for the probed and scattered fields for both grating components. This effect appears to a smaller extent in the pattern shown in Figure 10(B). However the

pattern in Figure 10(A) exhibits the predicted decaying amplitude side lobes. This indicates that near Bragg condition for scattering from the grating frequency component associated with the fundamental of the write beam interference pattern, the effects of scattering from other grating frequency components are negligible.

The results discussed above indicate that deviations from theoretically predicted scattering patterns will be observed when the interaction between the migrating charges and the electrostatic field are strong. This will occur for deep gratings and those with small spatial frequencies. The experimental conditions producing these conditions are long write times and large write beam crossing angles, respectively. Figure 11 shows an example of a scattering profile obtained after writing a grating for 15 minutes at a write beam crossing angle of 8.0^{o}. The asymmetry of the pattern and the strong side lobes resemble the shape of the pattern in Figure 11(C). Again this can be attributed to phase correlated contributions associated with scattering originating from different spacial frequency components of the grating interfering with the scattering from the fundamental component near its Bragg condition.

One way to reduce the interference effects produced by scattering from multi-Fourier component gratings is to create gratings with only a small population of charge relocation. This can be accomplished by reducing the writing time of the gratings. Figure 12 shows the small angle scattering patterns obtained for small amounts of charge relocation. For the small write angle results shown in part (A), a write time of two minutes could be used and still have a good fit between the experimental results and the predictions of Equation (138). For longer

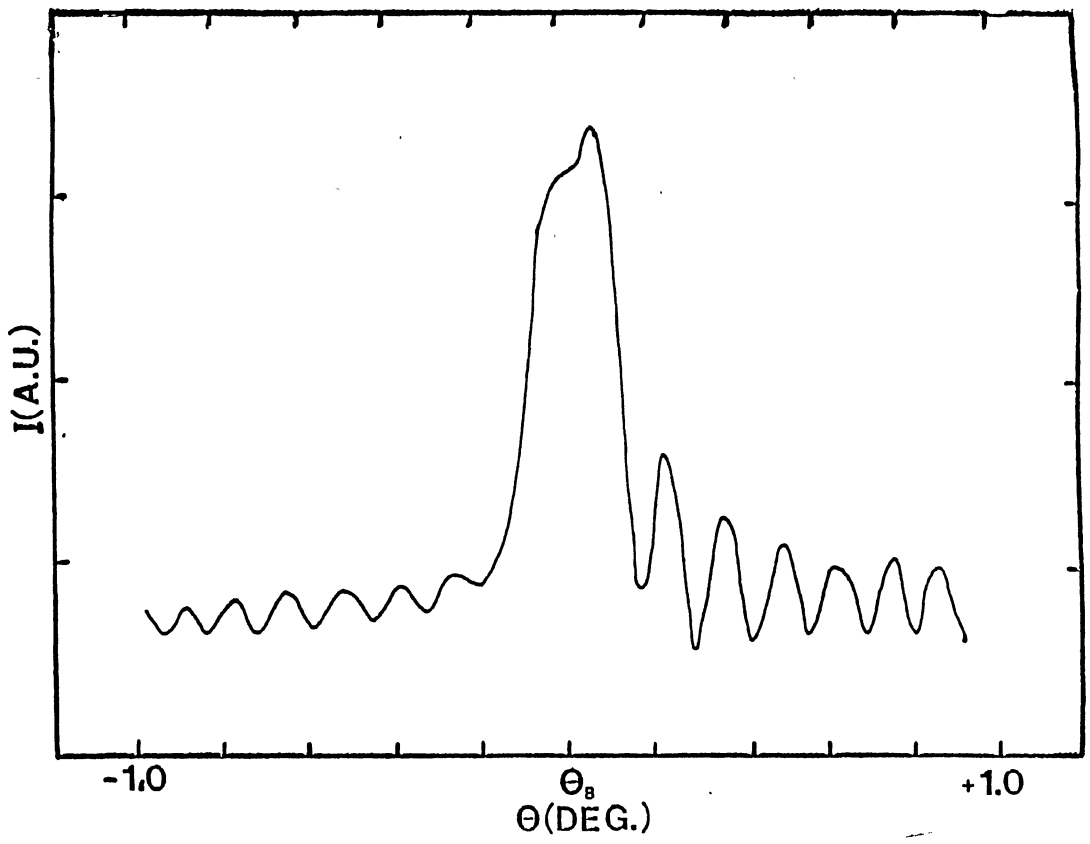

Figure 11. Small Angle Scattering Pattern for the First Spot in $LiNbO_3$ After a 15 Min Write Time at $\theta_W = 8^o$; $\theta_B = 7.5^o$

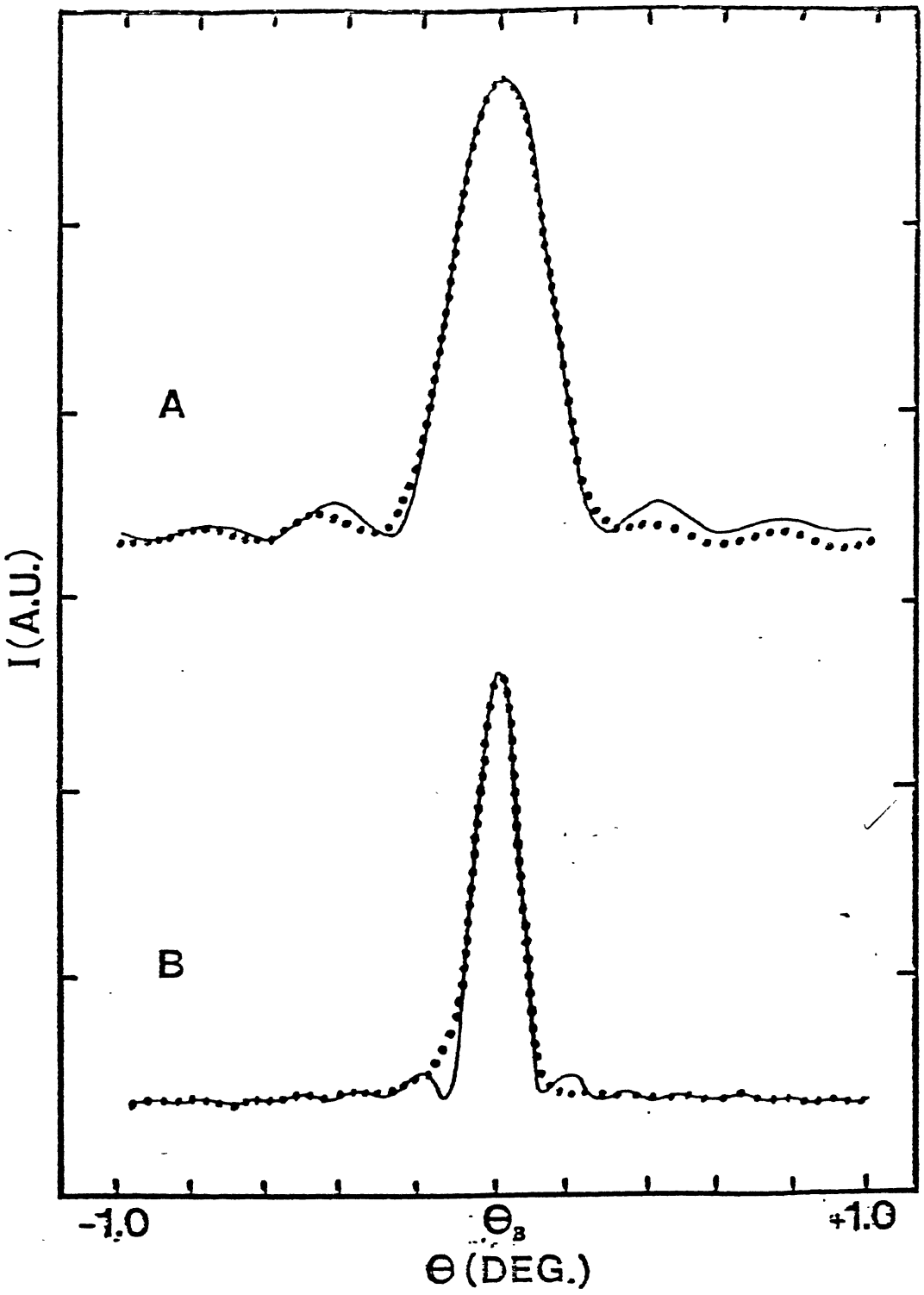

Figure 12. Small Angle Scattering Patterns for the First Spot in $LiNbO_3$. (A) $\Theta_W = 2.5^o$; $\Theta_B = 2.79^o$; $\Delta n = 3.48 \times 10^{-4}$; d = 370 μm; Write Time is 2 Min; (B) $\Theta_W = 8^o$; $\Theta_B = 7.5^o$; $\Delta n = 4 \times 10^{-4}$; d = 300 μm; Write Time is 20 Sec

write times, discrepancies between theory and experiment begin to occur. Part (B) of the figure shows similar results for a larger write angle. In this case the good fit shown between theory and experimental results could be obtained for write times of only 20 seconds or less. This demonstrates that the smaller grating spacing produced at larger write angles results in significant electrostatic field effects for smaller numbers of charges relocated compared to the effects seen for gratings with large spacings.

Results of Magnesium Doped $LiNbO_3$

Different dopings of magnesium in $LiNbO_3$ give different index of refraction modulation depths. The change in grating depth as compared with concentration of magnesium is shown in Figure 13. A write beam crossing angle of 4.0° and a write beam time of two minutes was used. The scattering pattern associated with the fundamental grating frequency, located at an angle of 6.0°, was then examined. The thickness of the grating formed in the magnesium doped samples stayed constant at d = 300 μm. The grating depth decreases as the concentration of magnesium increases. A grating depth of 17×10^{-4} was found for a concentration of 1.8% m/o magnesium. The grating depth decreased to 11×10^{-4} when the concentration of magnesium was increased to 3.6% m/o. The depth of the grating then appears to reach a threshold value for 5% m/o magnesium. At 5% m/o magnesium the grating depth was 4.1×10^{-4} and changed only slightly to 3.9×10^{-4} for a magnesium concentration of 8.8% m/o.

The data shown in Figure 13 agrees qualitatively with earlier data and confirms the 5% m/o threshold value of magnesium in $LiNbO_3$.

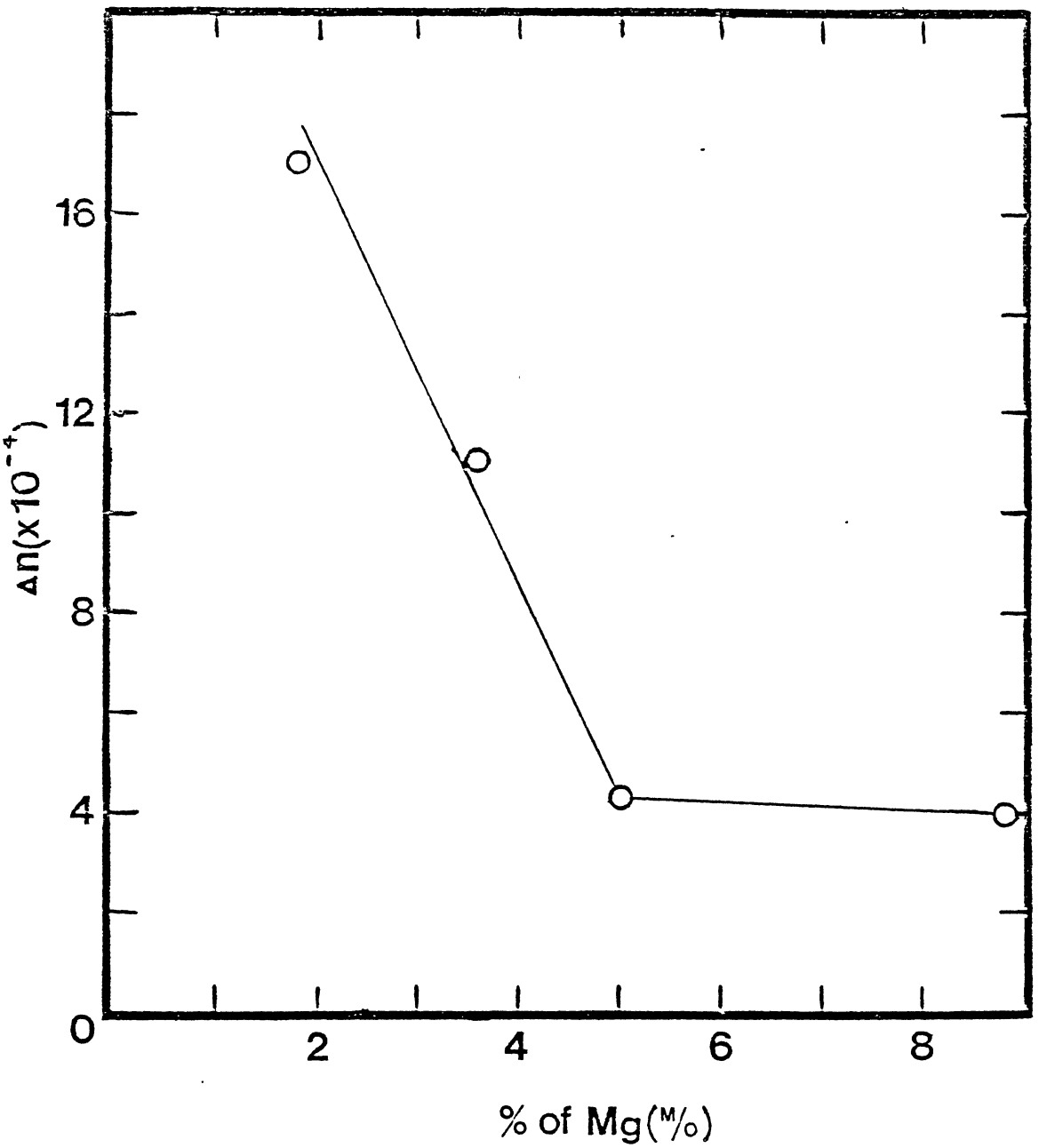

Figure 13. Change in Index of Refraction Modulation Depth with Change in Concentration of Magnesium in $LiNbO_3$ for a Write Beam Crossing Angle of 4.0° and a Write Time of 2 Minutes

The threshold level depends upon both the magnesium concentration and the lithium vacancy concentration in the crystal. When electrons are released in $LiNbO_3$ with a doping concentration of magnesium greater than 5% m/o, the Mg^{2+} ions act as a trapping site and the photorefractive effect is quenched. It should be noted at this time that the threshold Mg doping level is not a constant but depends upon the ratio of Mg ions to lithium vacancies [14]. Published results report that the damage resistance of lithium niobate is increased by a factor of 10 to 100 when the crystals are heavily doped with Mg [15]. For undoped $LiNbO_3$ a typical value of the index of refraction modulation depth is $\Delta n = 2 \times 10^{-4}$ and after introducing MgO, $\Delta n = 2 \times 10^{-5}$. From results obtained in this experiment, $\Delta n = 10^{-4}$. The thickness of the grating depth was d = 500 μm as given from the computer. This value of the grating thickness was too small to give an index of refraction modulation depth of $\Delta n \approx 10^{-5}$ as was anticipated. Therefore, it is concluded that the scattering pattern will give a value for the grating depth which is a factor of 10 greater than that obtained from the scattering efficiency. At this moment, the discrepancy in values of Δn extracted from the two methods are confined to dopings of magnesium but it is very probable that any material which quenches the photorefractive effect will give similar results.

Results of Proton Diffused $LiNbO_3$

The diffusion of protons into $LiNbO_3$ introduces deep traps for the migrating charges. Therefore, proton diffusion reduces the grating depth. The effect of diffusing protons into $LiNbO_3$ by means of soaking the sample in benzoic acid for varying periods of time is shown in

Figure 14. For a write beam crossing angle of 4.1^{o} and a write time of two minutes, the modulation depth ranges from 3.5×10^{-4} to 2.75×10^{-4} with a constant grating thickness d = 400 μm. For diffusion times of 2 days, 4 days, 8 days, and 14 days values of 3.5×10^{-4}, 3.15×10^{-4}, 3.13×10^{-4}, and 2.75×10^{-4} were obtained, respectively. Figure 15 shows the different decay times for the fundamental, first, and second harmonics of the write beams' interference pattern. Other than the fact that once again the different harmonics of the interference pattern have different decay rates, the decay rates of the proton diffused samples differ from the decay rates of the "nominally pure" samples. This indicates a different combination of processes in the charge transport. The scattering pattern for proton diffused $LiNbO_3$ at a write beam crossing angle of 4.5^{o} is shown in Figure 16.

The quenching of the photorefractive effect also takes place due to proton diffusion. The quenching happens somewhere under two days of proton diffusion. Earlier published papers on proton diffusion in $LiNbO_3$ gives index of refraction modulation depths of $\Delta n = 2.62 \times 10^{-5}$ [16]. As in Mg doped $LiNbO_3$, the effect is the same but not as drastic as earlier reports would indicate. The qualitative agreement of results can be attributed to the fact that the shape of the scattering pattern and the scattering efficiency behave the same. The discrepancy in values for the grating depth is once again attributed to the shape of the scattering pattern giving a different value for the modulation depth than that obtained from the scattering efficiency.

Results of Cu and Er Doped $LiNbO_3$

The fundamental, first, and second harmonics of the write beams'

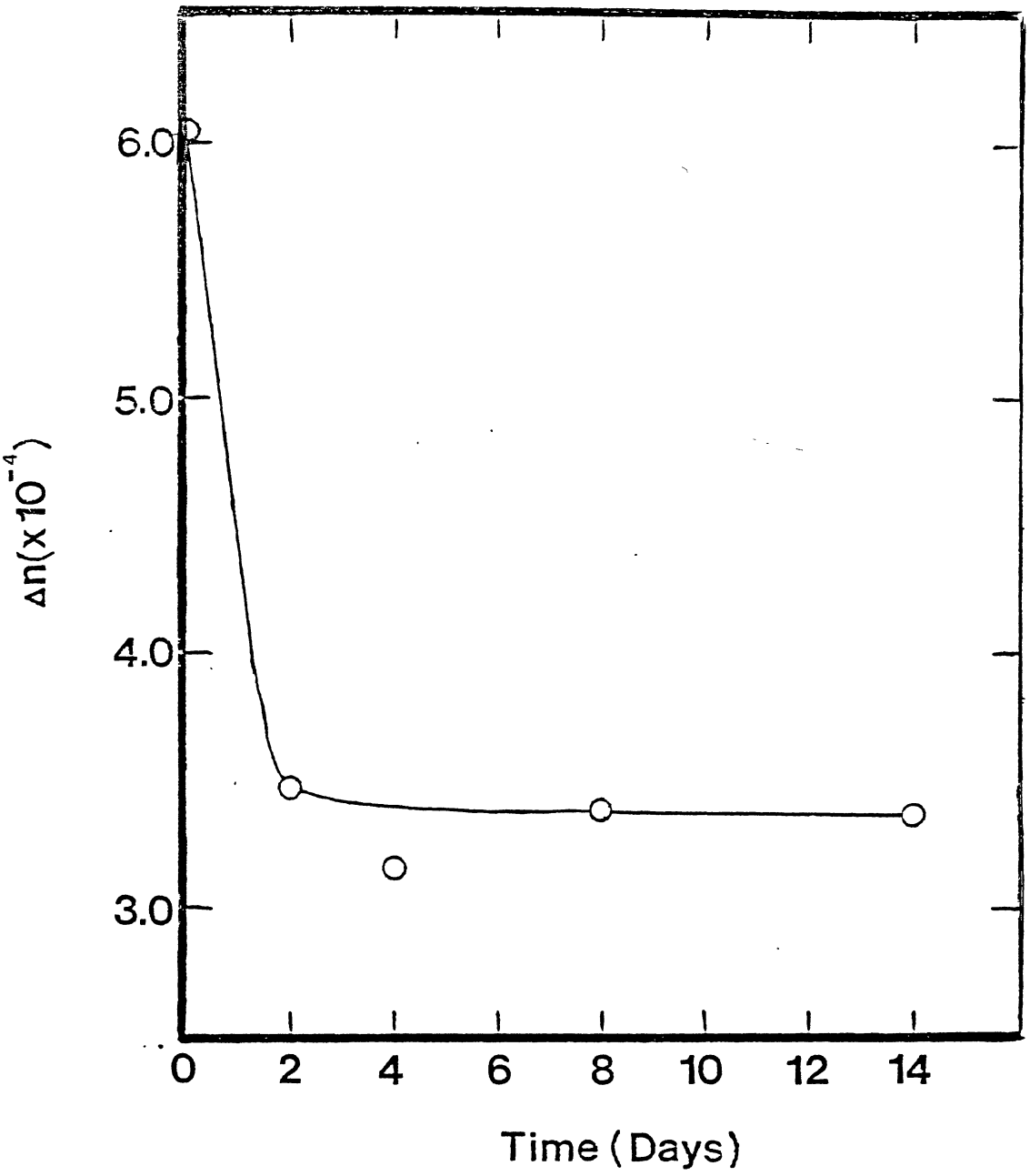

Figure 14. The Change in the Modulation Depth of $LiNbO_3$ with Respect to Proton Diffusion

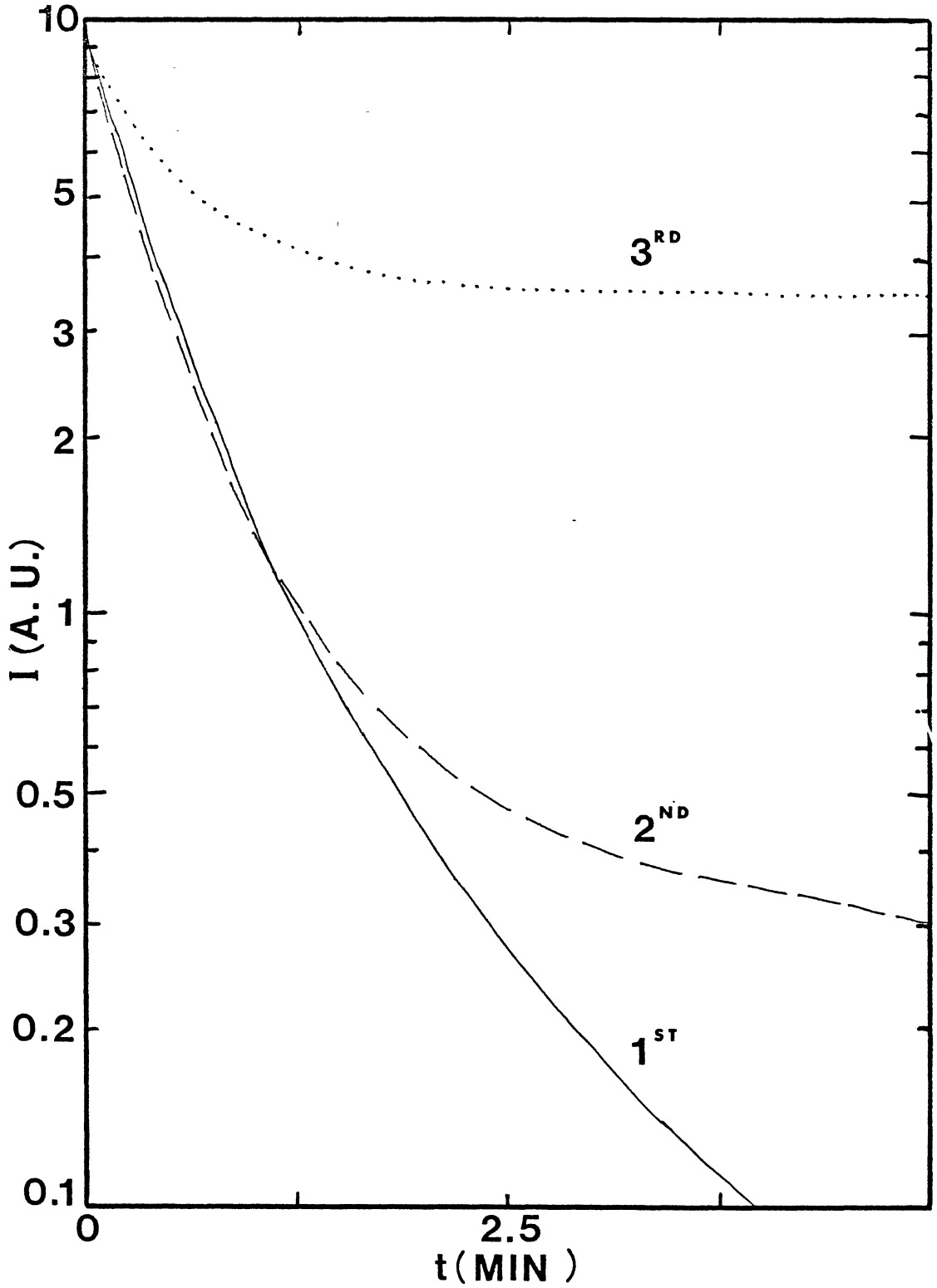

Figure 15. Decay for Fundamental, First, and Second Harmonies of the Write Beam's Interference Pattern in Proton Diffused $LiNbO_3$ for a Write Beam Crossing Angle of 4.2^{o}

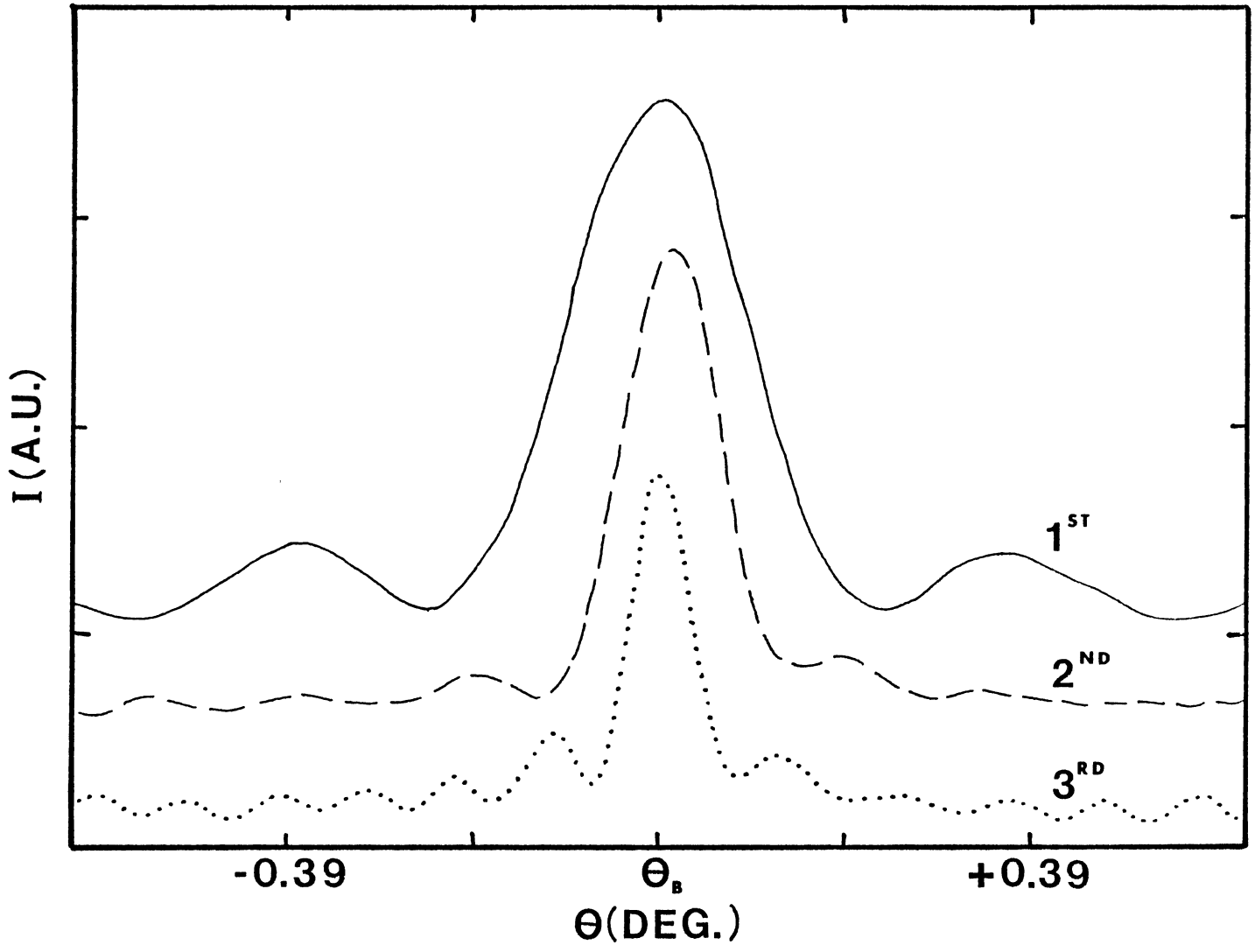

Figure 16. The Scattering Pattern for Proton Diffused $LiNbO_3$ at a Write Beam Crossing Angle of 4.5^{o}

interference pattern in copper doped $LiNbO_3$ also have different decay times. The decay rates are shown in Figure 17. The scattering patterns around the three primary scattering maxima for a write beam crossing angle of 4.5° are shown in Figure 18. The central peak of the scattering pattern becomes less broad as the higher harmonic frequencies of the grating are approached. In Figure 19, the small angle scattering patterns around the fundamental scattering maxima for varying write beam crossing angles are examined. As the write beam crossing angle is increased, the grating thickness and grating depth become small. For a write time of 30 seconds and a write beam crossing angle of 4.1°, the best computer fit for copper doped $LiNbO_3$ gives values for the depth and thickness of the grating at 14×10^{-4} and 100 μm, respectively. The copper enhances the photorefractive effect in $LiNbO_3$ by introducing charge carriers. The doping of copper increases the index of refraction modulation depth by a factor of 10 as anticipated.

Erbium doped $LiNbO_3$ was also examined and for a write time of 30 seconds and a write beam crossing angle of 4.1°, values for the grating depth and thickness were obtained. Equation (138) gave values of $\Delta n = 5.4 \times 10^{-4}$ and $d = 280$ μm. The Erbium produced no significant change in the grating depth and the results were as expected.

Figure 20 shows experimental results and theoretical fits for copper doped $LiNbO_3$,(A); Erbium doped $LiNbO_3$,(B); and proton diffused $LiNbO_3$,(C).

Results of Erasure

The effect of erasing the holographic grating formed in "nominally pure" $LiNbO_3$ was examined. A holographic grating was formed by crossing two write beams at an angle of 4.1° for one minute. The grating was

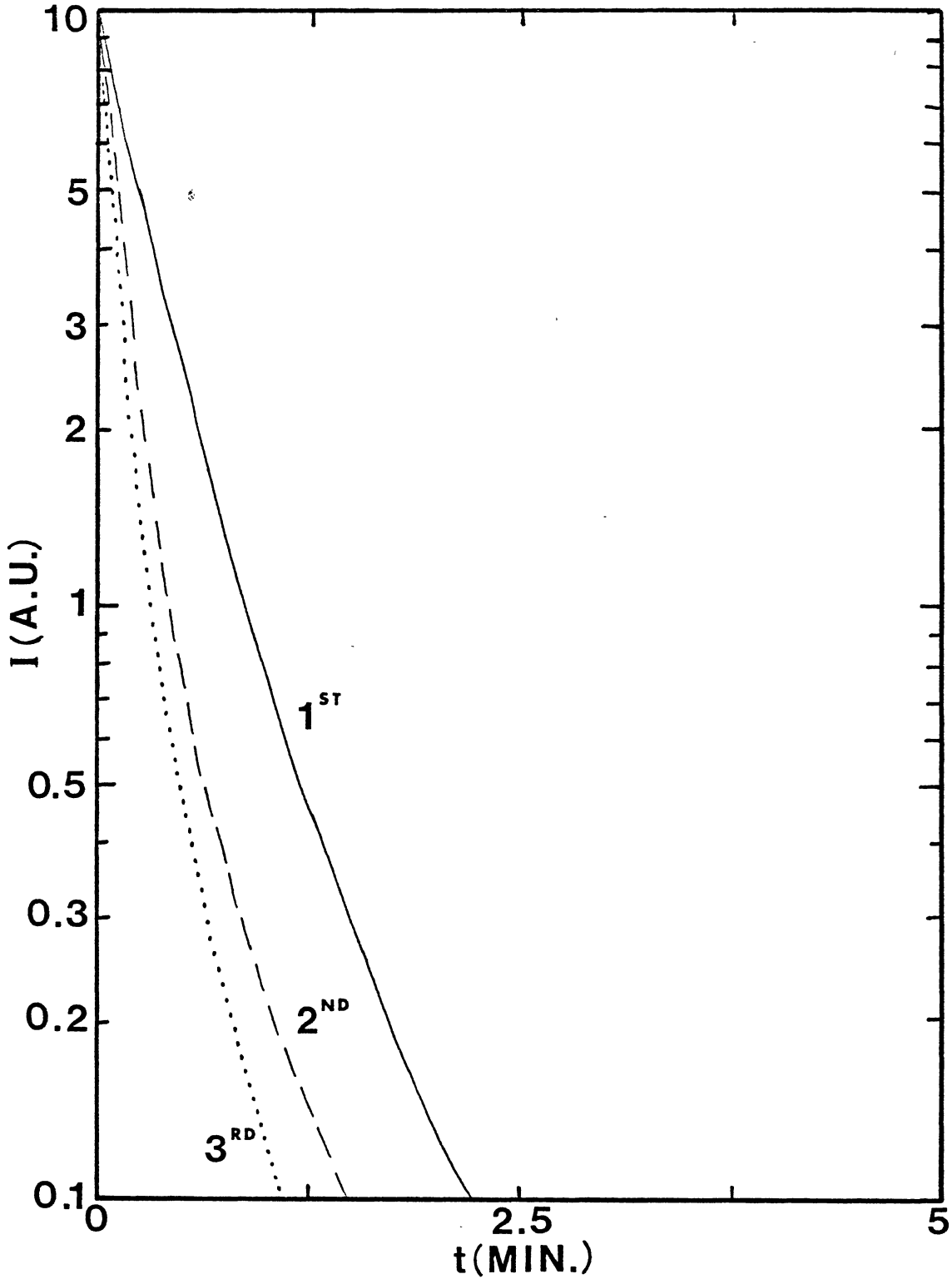

Figure 17. The Decay of the Three Primary Scattering Maxima in Copper Doped $LiNbO_3$ for a Write Beam Crossing Angle of 4.2^{o}

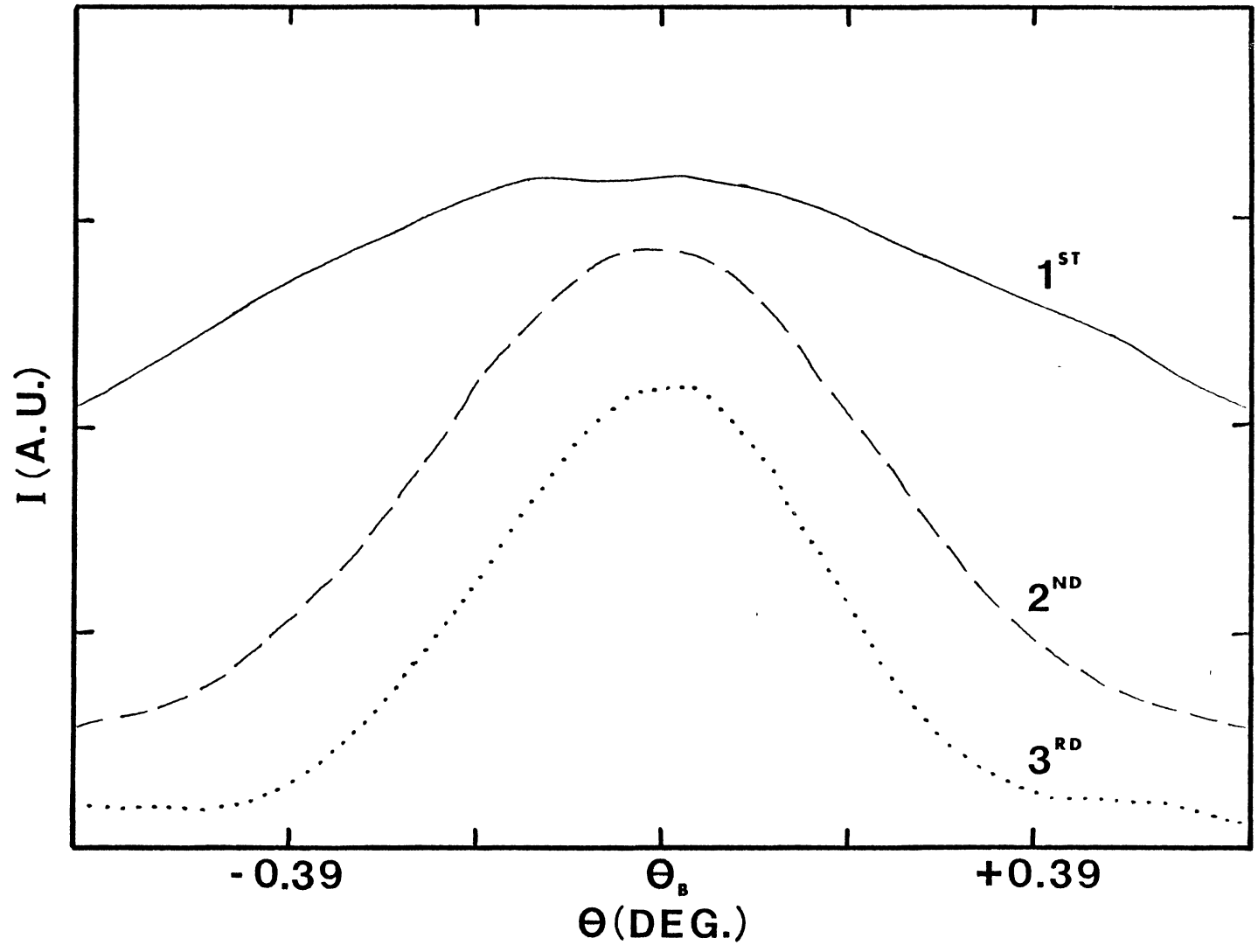

Figure 18. The Scattering Patterns Around the Three Primary Scattering Maxima in Copper Doped $LiNbO_3$ for a Write Beam Crossing Angle of 4.5^{o}

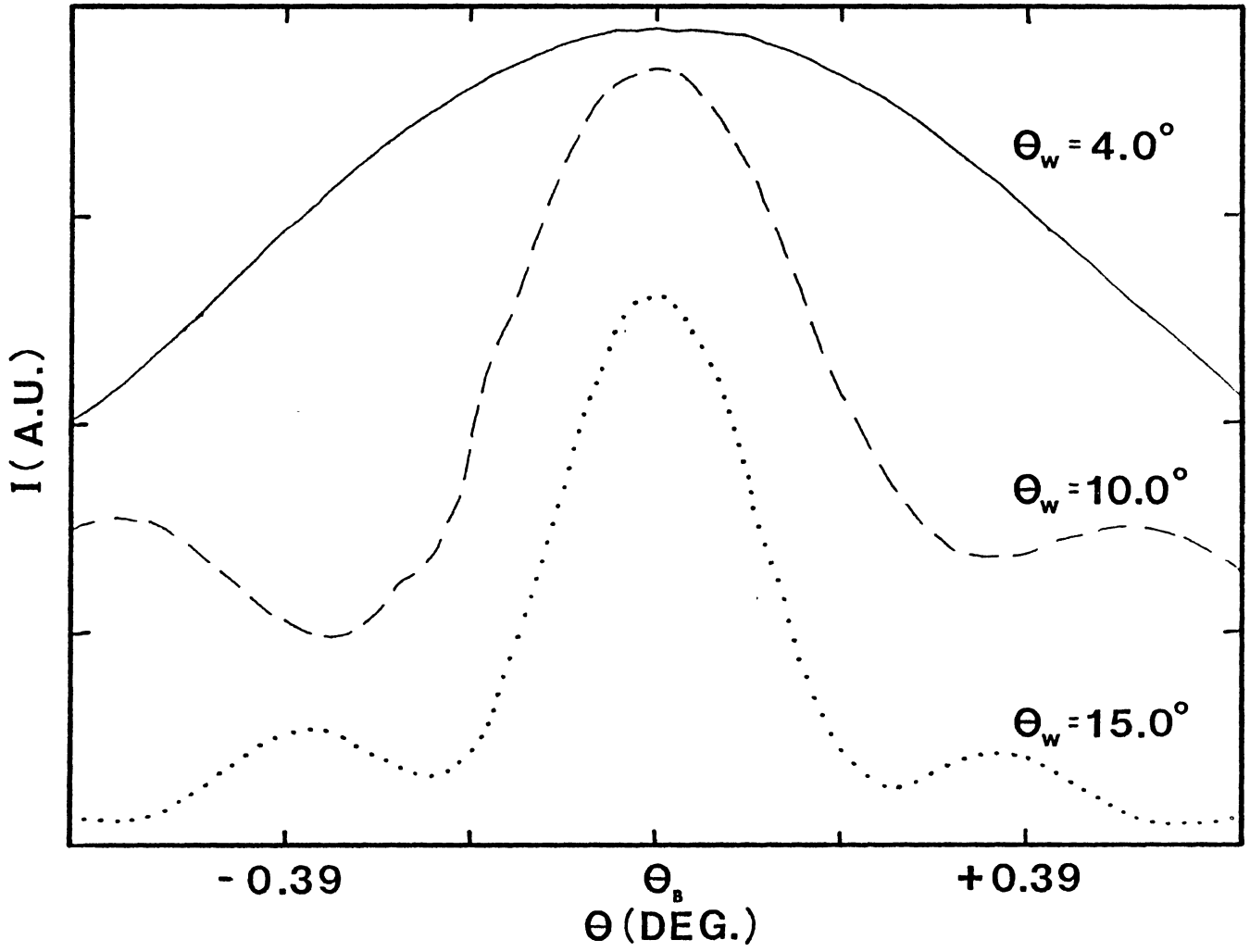

Figure 19. Small Angle Scattering Patterns for the First Spot in Copper Doped $LiNbO_3$. Different Write Beam Crossing Angles of 4.0°, 10.0° and 15.0° Were Used to Produce the Patterns

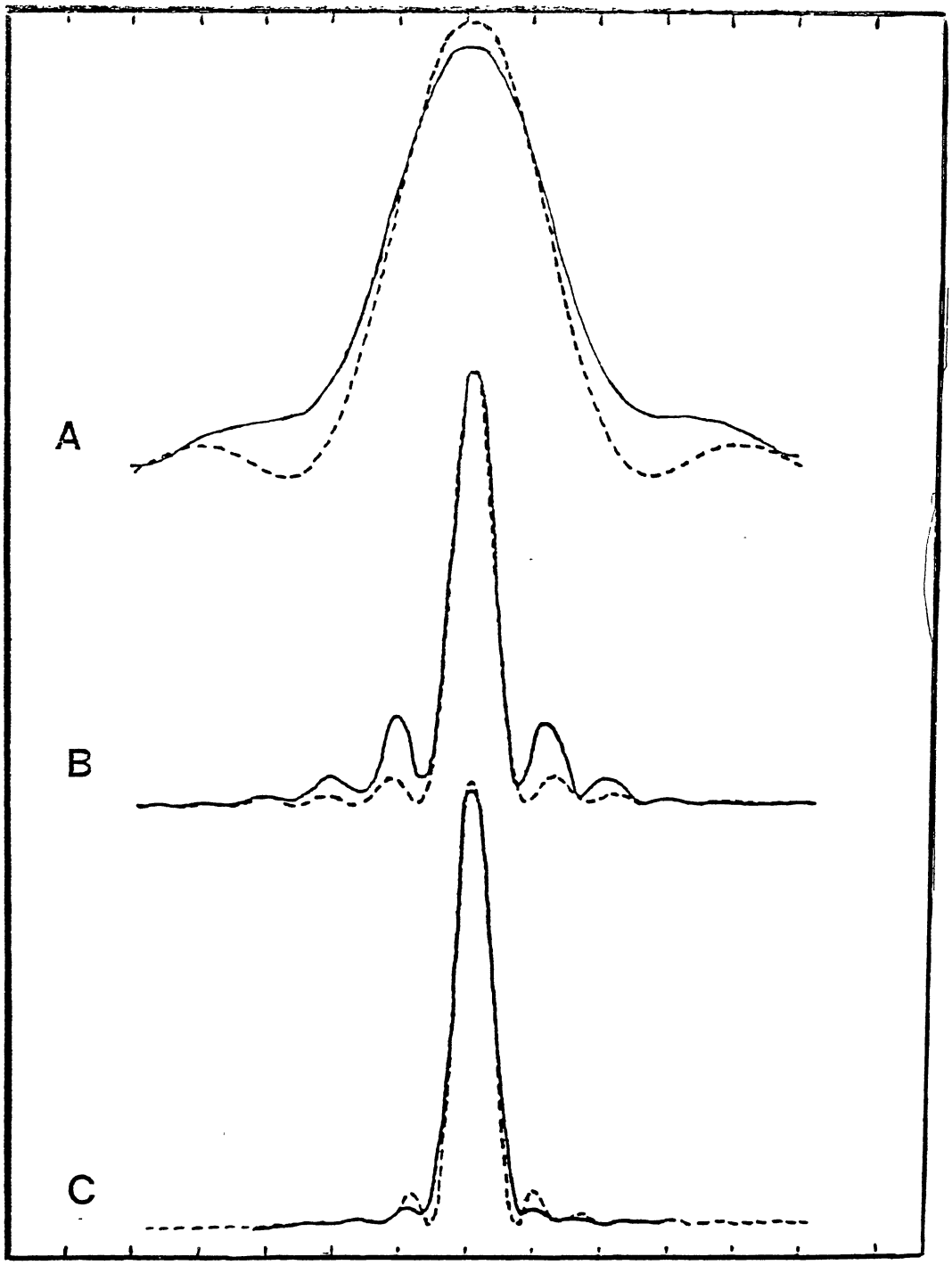

Figure 20. Experimental Results and Theoretical Fits for Copper Doped $LiNbO_3$,(A); Erbium Doped $LiNbO_3$,(B); and Proton Diffused $LiNbO_3$,(C)

partially erased and the best fit was found for the scattering profiles. Erasure was continued and values for the scattering efficiency, the grating depth, and the grating thickness were obtained.

Figure 21 demonstrates the effect of erasing the grating on the scattering efficiency. This data can be approximated by a double exponential curve. This curve originates from the presence of two different gratings having different types of charge dynamics [8].

Figure 22 is a plot of the index of refraction modulation depth as a function of the erasure time. The data in this case is approximated by a single exponential curve. The index of refraction modulation depth varies from $\Delta n = 2.73 \times 10^{-4}$ at no erasure to $\Delta n = 2.12 \times 10^{-4}$ after three minutes of erasure. Both the scattering efficiency and the grating depth were extracted from the same data run so it was assumed that Figures 21 and 22 would exhibit the same behavior. The discrepancy can be explained as follows: the accepted procedure for obtaining the index of refraction modulation depth as been to assume a constant grating thickness and to measure the scattering efficiency. Kogelnik derived an expression for describing the first order Bragg diffraction from a thick hologram refractive-index grating. In the case of shallow gratings, his result simplifies to

$$I_s \alpha |\Delta n|^2$$

where I_s is the intensity of the scattered signal beam and the grating depth (Δn) is the difference in the refractive index n between the peak and valley regions of the grating. Then using Equation (164) the grating depth can be determined. The scattering efficiency looks at a combination

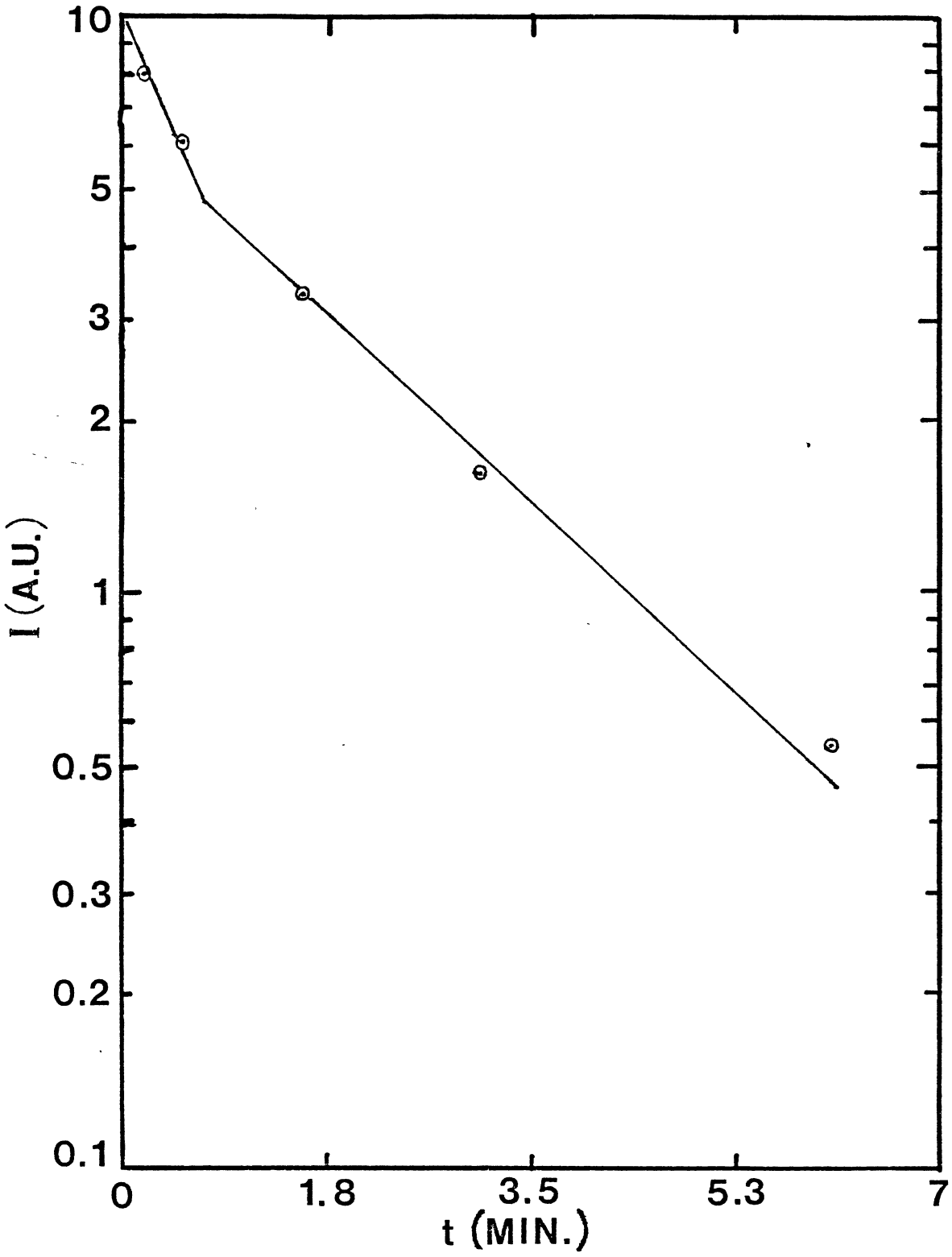

Figure 21. Scattering Efficiency During Erasure of the Grating

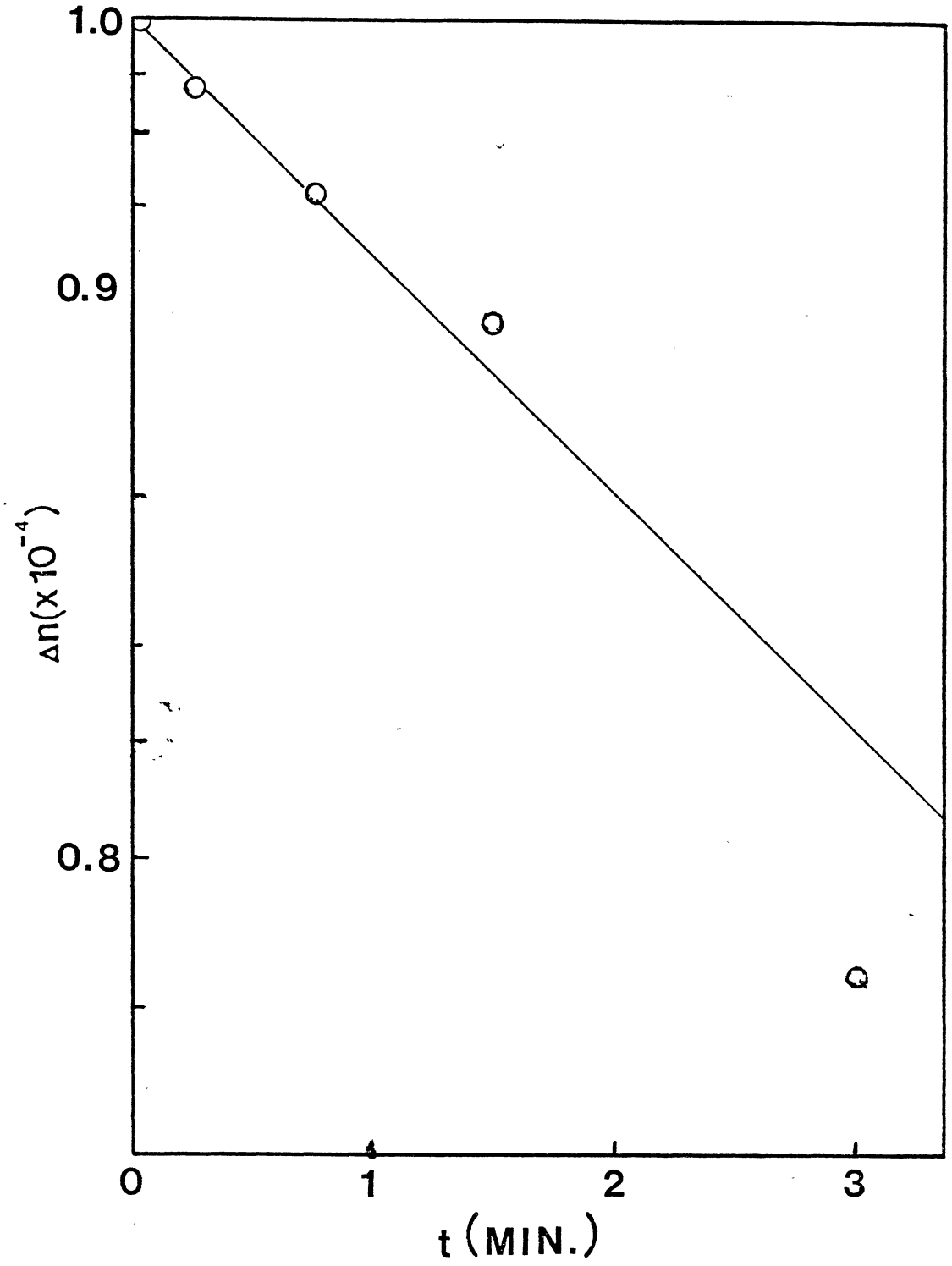

Figure 22. Change in the Index of Refraction Modulation Depth as the Grating is Erased

of grating vectors giving a double exponential curve. Using Equation (138), a single grating vector is examined during erasure giving a single exponential decay as a demonstrated in Figure 23. The decay rate of Figure 23 was expected to equal one of the components of Figure 22. This did not occur and at present this aspect is not understood.

It is observed from Figure 21 that some of the grating remains even after three minutes of erasure. This can be explained due to the fact the He-Cd laser beam was used in the erasure process. The energy levels before and after the migration of charges do not match and some of the energy levels remain full after erasure. In order to completely erase the holographic grating, white light or annealing of the sample should be used.

CHAPTER VI

SUMMARY AND CONCLUSIONS

Summary

The analysis of the total angular scattering patterns from laser-induced refractive index gratings in $LiNbO_3$ reveals intensity maxima in several directions. These maxima are associated with different components of a multi-Fourier component grating. This observation has not been investigated until now. An extension of Kogelnik's theory to a two frequency component grating predicts that the scattering efficiency at exactly Bragg condition for one component is not significantly affected by the presence of the other components, but scattering at other angles shows interference effects associated with scattering from different grating frequency components. Analysis of the small angle scattering patterns around the multiple scattering maxima observed for $LiNbO_3$ shows that this prediction is true for the lowest frequency grating component but it fails for the higher frequency components. A more rigorous theoretical treatment is needed for the higher frequency component in order to describe the nonlinear interaction between the migrating charges and the induced space charge field.

The dependence of the shapes of the small angle scattering patterns upon the write times has been reported before [11]. However, the technique of fitting computer simulated scattering patterns to experimentally

observed patterns has not been used before to obtain information about laser-induced grating parameters. The results presented here show that this technique is a very sensitive way to measure the grating thickness and the modulation depth. This method has significant advantages over the normal technique of measuring the scattering efficiency at the Bragg angle and relating the result to the index modulation depth by assuming a value for the effective thickness of the grating. Using the analysis of the scattering patterns, the value for the effective thickness of the grating does not have to be assumed. Along with the significantly greater degree of accuracy of determining the modulation depth and grating thickness, the analysis of the scattering patterns has the advantage of being useful over a wider range of experimental conditions than the range of validity of the more simplier relationship used in the Bragg angle scattering efficiency measurement (Equation (163)). In addition, the shapes of the central peak and the side lobes of the scattering pattern can provide information concerning interference effects from multiple scattering. These effects cannot be directly detected in simple Bragg angle scattering efficiency measurements and can contribute to erroneous results using this technique.

Scattering efficiency measurement at exact Bragg condition also suffer from experimental geometry problems. It has been shown that a detector acceptance angle of a few hundredths of a degree provided by a slightly converging or diverging signal beam can give erroneous results. This problem becomes very crucial for shallow gratings.

When doping $LiNbO_3$ for the purpose of quenching the photorefractive effect, it has been found that values for the grating depth and grating

thickness obtained from the scattering patterns differ from values obtained from the scattering efficiency. It has been suggested that this is due to the scattering efficiency looking at a combination of the fundamental, first, and second harmonics of the grating whereas the technique of the scattering pattern isolates one of the harmonics of the gratings. This assumption can also be applied to the effect of erasure upon the holographic grating.

Future Work

The application of the small angle scattering analysis technique on $LiNbO_3$ demonstrates the changes that occur in the scattering pattern as a function of write angle and write time. This is not where the research ends, but where it begins. The research to be done in the future is both exciting and challenging. The most obvious future research is the application of the small angle scattering analysis technique on other photorefractive materials. Another area is the discrepancy in the erasure data. The reason for obtaining a double exponential from the scattering efficiency versus a single exponential obtained from the small angle scattering analysis technique must be found. Using the same experimental set-up, defect resonance can be investigated. A grating is to be written with a wavelength corresponding to the absorption band of the impurity. The small angle scattering analysis pattern is then examined to see what effect writing on the writing band produces. Another area to investigate is the relationship between the study of decay dynamics [8], the scattering efficiency technique [10], and the small angle scattering analysis technique. Each technique is powerful by itself, but the techniques have never been combined.

Two new and relatively simple but enlightening experiments are microfluorescence and internal stark splitting. Microfluorescence is micro-Raman spectroscopy. A deep grating is formed in iron doped $LiNbO_3$. Then using the Raman technique, the wavelength of Fe^{2+} and Fe^{3+} absorption are used to scan across the grating and the emission is detected. This is a simple experiment to determine if areas of Fe^{2+} and Fe^{3+} exist. Internal stark splitting studies the splitting of the emission band due to the internal electric field set up inside the crystal after the grating is formed. External stark splitting has been investigated previously but internal stark splitting has not been investigated. These will provide additional information as to the processes occurring during the photorefractive effect.

REFERENCES

1. Ashkin, A., G. D. Boyd, J. M. Dziedzic, and R. G. Smith, Appl. Phys. Lett. 9, 72 (1966).

2. Chen, F. S., J. Appl. Phys. 40, 3389 (1969).

3. Johnston, W. D., Jr., J. Appl. Phys. 41, 3279 (1970).

4. Gunter, P., Phys. Rep. 93, 199 (1982).

5. Peterson, G. E., A. A. Ballman, P. V. Lenzo, and P. M. Bridenbaugh, Appl. Phys. Lett. 5, 62 (1964).

6. Lenzo, P. V., E. B. Spencer, and K. Nassau, J. Opt. Soc. Am. 56, 633 (1966).

7. Feinberg, J., D. Heimnan, A. R. Tanquay, Jr., and R. W. Hellwarth, J. Appl. Phys. 51, 1279 (1980); J. Appl. Phys. 52, 537 (1980); and J. Feinberg in "Phase Conjugation," edited by S. J. Fisher (Academic Press, New York, 1983), p. 218.

8. Tyminski, J. K. and R. C. Powell, J. Opt. Soc. B 2, 440 (1985).

9. Klein, J. M., J. Appl. Phys. In Press.

10. Kogelnik, H., Bell Sys. Tech. J. 48, 2909 (1969).

11. Staebier, D. L., W. Burke, W. Phillips, and J. J. Amodei, Appl. Phys. Lett. 26, 182 (1975); D. L. Staebier in "Holographic Recording Materials" edited by H. M. Smith (Springer-Verlag, Berlin, 1977), P. 101.

12. Digonnet, M., M. Fejer, and R. Byer, Optics Letters 10, 235 (May, 1985).

13. Demicheli, M., J. Botineau, P. Sibillot, D. B. Ostrowsky, and M. Papuchon, Opt. Commun. 42, 101 (1982).

14. Sweeney, K. L., L. E. Halliburton, D. A. Bryan, R. R. Rice, R. Gerson, and H. E. Tomaschke, Appl. Phys. Lett. 45, 805 (1984).

15. Bryan, D. A., Robert Gerson, and H. E. Tomaschke, Appl. Phys. Lett. 44, 847 (1984).

16. Holman, R. C., P. J. Cressman, and J. F. Revelli, Appl. Phys. Lett. 32 (5), 1 March 1978.

VITA

Michael Lynn Kliewer

Candidate for the Degree of

Master of Science

Thesis: THE PHOTOREFRACTIVE EFFECT IN $LiNbO_3$

Major Field: Physics

Biographical:

Personal Data: Born in Lincoln, Nebraska, May 21, 1960, the son of Donald L. and Edna M. Kliewer.

Education: Graduated from Putnam City High School, Oklahoma City, Oklahoma, in May, 1978; attended Oklahoma State University and received the Bachelor of Science Degree in May, 1983, with a major in Mechanical Engineering; completed the requirements for the degree of Master of Science at Oklahoma State University in May, 1986.

Professional Experience: Engineering Trainee, Southwestern Refining, May, 1982, to August, 1982; Engineering Intern, Western Electric, May, 1983, to August, 1983; Graduate Teaching Assistant, Oklahoma State University, August, 1983, to May, 1984; Graduate Research Assistant, Laser Spectroscopy Facility, Oklahoma State University, May, 1984, to present. Member of National Society of Professional Engineers, American Society of Mechanical Engineers, Society of Physics Students, and the Optical Society of America.